Research Square

Preprints are preliminary reports that have not undergone peer review.
They should not be considered conclusive, used to inform clinical practice,
or referenced by the media as validated information.

Hydroxysafflor yellow A ameliorates high-fat diet-induced hyperlipidemia by attenuating hepatic lipotoxicity and partially restoring the gut microbiota–intestinal barrier axis

Caiyou Xu
Department of Cardiology, Affiliated Hospital of Nanjing University of Chinese Medicine
Keman Ji
Department of Cardiology, Affiliated Hospital of Nanjing University of Chinese Medicine
Haoran Li
Department of Cardiology, Affiliated Hospital of Nanjing University of Chinese Medicine
Jiabo Zhang
School of No. 1 Clinical Medical, Nanjing University of Chinese Medicine
Manping Wu
Department of Cardiology, Affiliated Hospital of Nanjing University of Chinese Medicine
Chao Chen
The First Affiliated Hospital of Anhui University of Chinese Medicine
Ruge Niu
Department of Cardiology, Affiliated Hospital of Nanjing University of Chinese Medicine
Yuan Sun
Department of Cardiology, Affiliated Hospital of Nanjing University of Chinese Medicine
Chunling Liu
njliuchunling@163.com

Department of Cardiology, Affiliated Hospital of Nanjing University of Chinese Medicine

Article

Keywords: Hyperlipidemia, Hydroxysafflor yellow A, Gut microbiota, PI3K/AKT/HIF-1α, Inflammation, Oxidative stress

Posted Date: May 28th, 2026

DOI: https://doi.org/10.21203/rs.3.rs-9650845/v1

License: This work is licensed under a Creative Commons Attribution 4.0 International License.
Read Full License

Additional Declarations: No competing interests reported.

Version of Record: A version of this preprint was published at Scientific Reports on October 10th, 2026.
See the published version at https://doi.org/10.1038/s41598-026-67572-0.

Abstract

Background

Hyperlipidemia is a major risk factor for cardiovascular diseases. Accumulating evidence has demonstrated that the gut microbiota-liver axis exerts a crucial regulatory effect on lipid metabolism. Hydroxysafflor yellow A (HSYA), a major bioactive compound derived from *Carthamus tinctorius* L., exhibits anti-inflammatory and antioxidant properties. However, its lipid-lowering effects and underlying mechanisms remain unclear.

Methods

High-fat diet (HFD)-induced hyperlipidemia mouse model and palmitic acid (PA)-induced HepG2 cells were used to evaluate the therapeutic effects of HSYA. We detected lipid metabolic parameters, hepatic and renal function indexes, serum lipid profiles, oxidative stress markers, and inflammatory cytokines in mice of each group. Oil Red O staining was applied to analyze hepatic lipid accumulation, while 16S rRNA sequencing was used to determine gut microbiota composition. The protein expression of the PI3K/AKT/HIF-1α pathway and lipid metabolism-related pathways were determined via Western blotting. Network pharmacology and gutMGene-based analyses validated potential targets and pathways, with molecular docking serving as supplementary confirmation.

Results

HSYA significantly ameliorated body weight gain abnormalities, dyslipidemia, and hepatic steatosis induced by high-fat diet in each group of mice. HSYA reduced the levels of total cholesterol (TC), triglyceride (TG), low-density lipoprotein cholesterol (LDL-C), alanine transaminase (ALT), and aspartate transaminase (AST) in murine serum; it enhanced antioxidant capacity by increasing the activity of superoxide dismutase (SOD) in murine liver, and suppressed inflammatory responses by downregulating the expression of TNF-α, IL-6, and IL-1β in murine serum. HSYA also restored gut microbiota homeostasis, increased the abundance of beneficial bacteria (e.g., Bacteroidota and Verrucomicrobiota), and improved intestinal barrier integrity by upregulating the expression of ZO-1 and occludin. Mechanistically, HSYA ameliorated hyperlipidemia primarily by modulating the PI3K/AKT/HIF-1α signaling pathway, accompanied by partial restoration of gut microbiota and intestinal barrier function. These findings were further supported by in vitro experiments and bioinformatics analyses.

Conclusions

HSYA alleviates HFD-induced dyslipidemia and hepatic steatosis by suppressing hepatic inflammation and lipogenesis via PI3K/AKT/HIF-1α signaling pathways and regulating the gut microbiota–gut barrier–liver axis. This study elucidates the underlying mechanisms of HSYA in ameliorating hyperlipidemia and hepatic steatosis, and offers experimental and theoretical evidence for its clinical potential in the treatment of metabolic disorders.

Introduction

Hyperlipidemia (HL) is a disorder of lipid metabolism characterized by elevated levels of total cholesterol (TC), triglycerides (TG), and low-density lipoprotein cholesterol (LDL-C), and/or decreased levels of high-density lipoprotein cholesterol (HDL-C). This condition is a major risk factor for obesity, type 2 diabetes mellitus, nonalcoholic fatty liver disease, and atherosclerotic cardiovascular disease[1]. The global prevalence of metabolic diseases has been increasing steadily in recent years. As of 2019, the age-standardized mortality rate attributable to HL was lower only than that of hypertension and obesity[2]. Patients with HL often require long-term pharmacological treatment. Currently available lipid-lowering agents, including statins and fibrates, are effective but may be associated with adverse effects such as hepatotoxicity, nephrotoxicity, and myotoxicity during prolonged use[3]. This imposes a substantial socioeconomic burden. Therefore, there is an urgent need to develop alternative lipid-lowering therapies with improved efficacy and fewer adverse effects.

The PI3K/Akt signaling pathway serves as a central regulator of cellular metabolism and function and plays a critical role in maintaining energy homeostasis[4]. Under hyperlipidemic conditions, impairment of this pathway is closely associated with dysregulated hepatic lipid metabolism. Activated Akt phosphorylates downstream targets, including glycogen synthase kinase-3β (GSK-3B), thereby modulating the activity of sterol regulatory element-binding protein-1c (SREBP-1c) and promoting fatty acid and cholesterol synthesis[5]. Meanwhile, the PI3K/Akt signaling pathway also regulates the transcriptional activity of peroxisome proliferator-activated receptor γ (PPARG), thereby coordinately modulating lipid storage and catabolism[6]. However, under sustained metabolic stress, aberrant activation of the PI3K/AKT pathway may contribute to excessive lipogenesis, inflammatory activation, and hepatic steatosis. Therefore, normalization of aberrant PI3K/AKT signaling may represent a potential therapeutic strategy for hyperlipidemia. Recent research indicates that the PI3K/Akt pathway serves a dual function in both intestinal and metabolic processes. In the intestine, its activity is essential for minimizing the translocation of intestinal endotoxin lipopolysaccharide (LPS), preserving the integrity of the epithelial barrier, and safeguarding the tight junction proteins Occludin and Zonula occludens-1 (ZO-1) from inflammatory damage[7]. In the HL model, it coordinates liver lipid synthesis and intestinal barrier function through the above-mentioned mechanism, constituting the core link to improve metabolic disorders.

The PI3K/Akt signaling pathway may regulate HIF-1α through mTOR, and mTOR may alter the level of HIF-1α after protein transcription. HIF-1α is a key regulator of cellular responses to metabolic stress. While its activation is known to promote angiogenesis and erythropoiesis[8,9], increasing evidence indicates that under hyperlipidemic conditions, HIF-1α activation contributes to glycolytic reprogramming and inflammatory responses, thereby promoting hepatic lipid accumulation[10,11]. The heterodimeric transcription factor HIF-1, consisting of the oxygen-sensitive and unstable HIF-1α subunit and the structurally stable HIF-1β subunit, plays a vital role in glycolysis and the transcription of inflammatory genes, including IL-1β[12]. The transcriptional activity of HIF-1 is primarily determined by the

stability of HIF-1α[13]. Under metabolic stress conditions, stabilized HIF-1α contributes to hepatic lipid accumulation by promoting metabolic reprogramming and inflammatory responses[14,15]. Therefore, targeting the stability or transcriptional activity of HIF-1α represents a promising strategy for intervening in HL-associated hepatic lipid accumulation.

Gut microbiota and intestinal barrier integrity are increasingly recognized as key regulators of host lipid metabolism and systemic inflammation. The intestinal microbiota enhances the expression of intestinal mucin through the production of short-chain fatty acids (SCFAs), thereby promoting the intestinal mucosal immune response. This immune system extends to other organs via multiple pathways. HIF, particularly HIF-1α, are recognized as the primary regulators of mucin expression. These metabolites elevate the oxygen consumption of intestinal cells, which stabilizes HIF-1 and activates the HIF-1 response within this tissue[16]. The activation of HIF-1 stimulates the production of MUC2 in intestinal goblet cells by generating mucus, antimicrobial peptides and expressing tight junction proteins, thereby promoting barrier function[17,18]. However, HIF-1 expression is excessively upregulated in response to a high-fat diet (HFD). In a rat model of thoracic aortic endothelial cell atherosclerosis induced by oxidized low-density lipoprotein, the complex signaling interactions between HIF-1 and the NF-κB pathway result in the upregulation and phosphorylation of HIF-1. This excessive activation subsequently initiates the transcription and expression of downstream inflammatory factors[19], this will produce excessive bacterial LPS, thereby causing damage to the intestinal barrier[20], accelerate the progression of atherosclerosis[21]. The same fatty acid oxidation promotes hepatic urate synthesis by activating the HIF-1α-NT5C2/XDH pathway, which links lipid metabolism to HU[22]. Thus, balancing the intricate crosstalk among gut microbiota, intestinal barrier, and the PI3K/Akt/HIF-1 signaling pathway has become increasingly crucial.

Hydroxysafflor yellow A (HSYA) is a clinical agent derived from the flowers of *Carthamus tinctorius* L. As one of its main active components, HSYA possesses notable antioxidant properties and is widely used in the treatment of acute ischemic stroke[23,24]. Patients with HL frequently demonstrate compromised antioxidant defense mechanisms, characterized by reduced concentrations of antioxidants, such as vitamins E and C, in the bloodstream, increased levels of lipid peroxidation products, and heightened systemic oxidative stress. Research indicates that HSYA effectively addresses diabetic nephropathy by mitigating oxidative stress and inflammation[25]. However, its impact on HL remains uncertain. By investigating the role of HSYA in the PI3K/Akt signaling pathway, as well as its effects on the microbiota and HIF-1α, we identified its potential therapeutic value for HL and proposed a corresponding mechanism. This study utilized in vitro and in vivo experiments, along with network pharmacology, to examine the transformation process of intestinal microbiota metabolites and to elucidate the molecular mechanisms through which HSYA and microbiota metabolites influence the progression of HL.

Materials and methods

Reagents

HSYA (purity ≥ 98.0%) was obtained from Bidepharm (Shanghai, China, BD134236). Primary antibodies against p-PI3K, PI3K, IL-6, IL-1β, iNOS, and HIF-1α were purchased from Cell Signaling Technology (CST, USA). Antibodies against p-NF-κB p65, NF-κB p65, p-AKT, AKT, TNF-α, and SREBP-1c were obtained from Abmart. Antibodies against ZO-1 and Occludin were acquired from Hua'an Biological (China). β-actin antibody was obtained from Affinity Biosciences (USA). Goat anti-mouse and anti-rabbit IgG secondary antibodies were supplied by Epizyme Biotechnology. CCK-8 reagent (Cat. No. K1018) was purchased from APExBIO (Houston, USA). Oil Red O staining kit, RIPA buffer, PMSF, phosphatase inhibitor cocktail, and BCA kit were obtained from Servicebio (Wuhan, China). TC, TG, and SOD kits were provided by Nanjing Jiancheng Bioengineering Institute (Nanjing, China). MDA kit was acquired from Beyotime Biotechnology (Shanghai, China). Biochemical kits for ALT, AST, TC, TG, HDL-C, LDL-C, urea, Crea, and UA were purchased from King Biotechnology (Zhejiang, China). TNF-α, IL-6, and LPS ELISA kits were obtained from biorbyt (UK).

Animal Model Establishment and Sampling

Six-week-old male C57BL/6J mice, weighing between 18 and 22 g, were obtained from China SPF (Suzhou) Biotechnology. (Quality Certification: SCXK (Su) 2022-0006). The mice were housed in an environment maintained at a temperature of (23 ± 2) °C, with a humidity of 55%±5%, and subjected to a 12-hour light-dark cycle, with unrestricted access to food and water. All experimental procedures adhered strictly to the recommendations outlined in the "Guidelines for the Care and Use of Laboratory Animals." The Laboratory Animal Ethics Committee of the Affiliated Hospital of Traditional Chinese Medicine, Nanjing University of Chinese Medicine, approved all animal experiments (No. 2025DW-063-01; Date: 2025-06-12). The safety of the administration was verified through literature review and pre-experimental assessments prior to the formal study. Following one week of acclimatization, the mice were randomly assigned using a random number table to five groups (n = 8), and the following protocol was implemented over 8 weeks: free access to diet and water, with HFD and normal-fat diet (NFD) replaced approximately every three days. The NC group served as the blank control, receiving a normal diet. The HFD group was fed a 60% high-fat diet. The L-HSYA group was administered an intraperitoneal injection of 2.5 mg/kg/d HSYA along with the 60% high-fat diet, while the H-HSYA group received an intraperitoneal injection of 7.5 mg/kg/d HSYA with the same diet. The atorvastatin (ATV) group received a 60% high-fat diet supplemented with ATV at a dosage of 2.6 mg/kg/d as the positive control[26,27]. The NFD group and the HFD group received injections of normal saline, administered according to the body weight of the mice. The 60% high-fat diet was supplied by Shuyu diet Biology. Given the excellent water solubility of HSYA, it was directly dissolved in sterile 0.9% physiological saline for subsequent administration. The dose of ATV was equivalent to the clinical adult dosage of 20 mg per day. Its suspension was prepared by mixing and grinding the original drug (Lipitor, 20 mg per tablet, Pfizer) with sterile 0.9% normal saline, calculated based on the body surface area of the experimental animals. At the end of the experiment, 14-week-old C57BL/6J mice were fasted for 12 hours, rapidly anesthetized with 4% − 5% isoflurane in an induction box, then adjusted to 1% − 2% isoflurane for maintenance with a mask (isoflurane from RWD Life Science). After blood collection from the retrobulbar venous plexus under

deep isoflurane anesthesia, death was confirmed by permanent cessation of respiration and heartbeat as well as fixed and dilated pupils. The study is reported in compliance with the Animal Research: Reporting of In Vivo Experiments (ARRIVE) guidelines[28]. Liver and epididymal fat tissues were collected, washed repeatedly, weighed in pre-cooled normal saline, and their liver weight, epididymal fat weight, liver index and epididymal fat index were calculated. Liver tissues were snap-frozen in liquid nitrogen and stored at -80°C for subsequent use.

Measurement of Mouse Body Weight and Liver index

Throughout the experiment, the body weight of the mice was measured at fixed intervals of three days, and the data were meticulously recorded. Blood glucose fluctuations were assessed biweekly. Prior to sampling, glucose (2.0 g/kg) was administered via intraperitoneal injection for the IPGTT test. Blood glucose levels were determined through tail tip sampling at 0, 15, 30, 60, and 120 minutes, with measurements taken using a blood glucose meter.

Carotid artery ultrasonography in mice

The bilateral common carotid arteries, carotid bifurcations and proximal internal carotid arteries of mice were examined by high-resolution color Doppler ultrasound. After anesthesia, the mice were placed in the supine position, and the carotid intima-media thickness was measured on the distal wall within 1 cm of the distal end of the bilateral common carotid arteries.

Biochemical analysis of mouse serum

The levels of ALT, AST, urea, creatinine, uric acid, TC, TG, HDL-C, and LDL-C in mice were measured using the Beckman AU480 fully automated biochemical analyzer from the United States. Concurrently, in vivo activity levels were assessed with SOD detection kits (Nanjing Jiancheng Bioengineering Institute, Nanjing, China) and MDA detection kits (Beyotime, Shanghai, China). Additionally, mouse serum was analyzed for TNF-α, IL-6, and LPS using ELISA kits, with all procedures conducted according to the provided instructions.

Liver oil red staining and histological analysis of Epididymal fat

Fresh epididymal fat samples were fixed in 4% paraformaldehyde to prepare 5-μm paraffin sections. Following dewaxing and hydration, tissue morphology was examined using hematoxylin-eosin (H&E) staining. Additionally, specimens from the middle lobe and left lateral liver tissue of mice were fixed in 4% paraformaldehyde and subsequently embedded in paraffin to prepare frozen liver tissue sections. The 10-micron thick frozen sections were stained with oil red O according to the instructions provided

with the Wuhan Sewell kit and were sealed with glycerol gelatin. The lipid droplet content in the liver tissues of mice from each group was observed using an optical microscope.

Gut microbiota and intestinal barrier analyses

Colonic contents from mice were collected, and fecal genomic DNA was extracted. Primers were employed to amplify the V3-V4 regions of bacteria using 515F (CCTAYGGGRBGCASCAG) and 806R (GGACTACNNGGGTATCTAAT). Each PCR mixture contained 15 μL of Phusion High-Fidelity PCR Master Mix, 0.2 μM primers, and 10 ng of genomic DNA templates. The quantitative library was purified and sequenced on the NovaSeq6000 or DNBSEQ-G99 platform (Beijing Novogene Technology Co., Ltd., China). The DADA2 module in QIIME2 software (version QIIME2-202,202) was utilized to reduce data noise and obtain the initial amplicon sequence variants. Species annotation was performed using the Silva138.1 database. Both alpha and beta diversity analyses were conducted, employing the Chao1 index, the number of observed features, the Shannon and Simpson indices, and non-metric multidimensional scaling analysis (NMDS) to evaluate sample abundance across different taxonomic levels (phylum, family, and genus). Linear discriminant analysis effect size (LEfSe) was applied to identify species with significant abundance differences between groups. The function of the intestinal microbiota was predicted using phylogenetic Study 2 (PICRUSt2).

Western blot analysis

Tissue samples were treated with RIPA lysis buffer supplemented with PMSF and phosphatase inhibitors (Servicebio, Wuhan, China). Following lysis on ice, samples were centrifuged at 12,000 rpm for 20 minutes at 4°C, and the supernatant was aspirated. The protein concentration in the supernatant was quantified using a BCA detection kit. Samples containing 20μg of protein were separated by sodium dodecyl sulfate-polyacrylamide gel electrophoresis, transferred to PVDF membranes (Millipore, Merck, Germany), and sealed at room temperature for 1.5 hours. The primary antibody was incubated overnight. The following day, the bands were incubated with the corresponding secondary antibody for 60 minutes, and the signal was developed using an ECL detection reagent (Beyotime, Shanghai, China). Relative band intensity was quantified using Image J software (National Institutes of Health, Bethesda, Maryland, USA).

Cell culture

Human hepatocellular carcinoma (HepG2) cells were obtained from the Central Laboratory of Jiangsu Provincial Hospital of Chinese Medicine. These cells were cultured in DMEM medium supplemented with 10% FBS and 1% antibiotics, consisting of 100 U/ml penicillin and 100 U/ml streptomycin. The cultures were maintained in a 5% carbon dioxide incubator at 37℃ (ThermoFisher Scientific, USA). The culture medium was changed based on the growth conditions of the cells. The experiment commenced when the cell density reached 85–90%.

Cell survival rate

When the density of HepG2 cells reached 85%-90%, trypsin was employed for enzymatic digestion, followed by the inoculation of the cells into 96-well plates at a density of 10^4 cells per well. HSYA was dissolved in DMEM medium. After cell adhesion, a 0–1 mM solution of PA or a 0-640 μM HSYA solution was added to each group of five replicate wells. After 24 hours of incubation, 10 μl of CCK8 solution was introduced into each well. Absorbance was measured at 450 nm one hour later. The cell survival rate in response to varying PA concentrations and the toxic effects of HSYA on HepG2 cells were calculated. The appropriate concentration of PA was selected for modeling, and different concentrations of HSYA were utilized to assess changes in cell activity post-modeling.

Cellular lipids

HepG2 cells (5×10^5 cells per well) were plated in six-well plates and incubated for 24 hours. The cells were then treated with 0.5 mM PA, in combination with 80 μM, 160 μM, and 320 μM HSYA and 5 μmol/L ATV. Following a 24-hour incubation, the cells were washed three times with PBS and fixed in 4% paraformaldehyde for 20 minutes, followed by PBS washing. Subsequently, the cells were dehydrated with 60% isopropyl alcohol (30 seconds), stained with Oil Red O at 25°C for 1 hour, and washed thrice with 60% isopropyl alcohol and PBS. Imaging was performed using an inverted phase contrast microscope (Nikon Precision (Shanghai, China).

In a separate experiment, TC and TG levels in the supernatant of HepG2 cells were assessed using commercial kits (Nanjing Jiancheng Institute of Bioengineering, Nanjing, China) following the manufacturer's instructions. After thorough mixing by shaking the 96-well plate, incubation was carried out at 37°C for the specified duration. Absorbance values of each well were determined using a microplate reader, and TC and TG concentrations for each group were calculated based on the OD values obtained.

Quantitative real-time PCR

The RNA extraction kit (R711), DNA reverse transcription kit (RT333), and PCR amplification kit (Q312) were all purchased from Nanjing Vazyme Biotechnology. Operations must be carried out strictly in accordance with the instructions. Primers are listed in Table 1.

Table 1
Sequences of primers for qPCR

SREBP-1c	**Forward primer (5'-3')**	**Reverse primer (5'-3')**
	TTCTTCGTGGATGGGGACTG	**GTCACACAGTTCAGTGCTCG**
FASN	GGTCTACTACGCCTCCCTCA	GTTGGAAGGCACATCCCAGA
PPARA	GCTGGTGTATGACAAGTGCG	TGACATCCCGACAGAAAGGC
CPT1A	TTCAGTTCACGGTCACTCCG	GGGTCGATCTTGGCGTACAT
IL-6	TGAGGAGACTTGCCTGGTGAA	CAGCTCTGGCTTGTTCCTCAC
TNF-α	TATCCTGGGGGACCCAATGT	AAAAGAAGGCACAGAGGCCA
ACTIN	ACTGTCGAGTCGCGTCC	CCCACGATGGAGGGGAATAC

Integrated bioinformatics analysis

Screening of intestinal microbiota metabolites and drug and disease targets

Gut microbiota metabolites and associated target genes were sourced from the gutMGene v2.0 database. These metabolites were subsequently converted into SMILES format utilizing the PubChem database. The potential targets of these metabolites were predicted using the SEA and STP databases, restricting the species to Homo sapiens and applying a screening criterion of probability > 0. A Venn diagram was employed to identify overlapping targets predicted by both methods, which were then selected as the final candidate target set. For details regarding the database sources and software utilized, please refer to the relevant sections Table S1.

Using "Hyperlipidemia" as the keyword, we searched for disease targets associated with it in the GeneCards, DisGeNET, and OMIM databases. The overlapping disease targets identified across these three databases were illustrated using Venn diagrams and defined as the final set of HL-related targets. Targets related to HSYA were obtained from the TCMSP and STP databases. The screening criteria for TCMSP included an oral bioavailability of ≥ 30% and a drug-likeness score of ≥ 0.18. In STP, a retention probability threshold of > 0.1 was applied.

Construction of protein-protein interaction (PPI) networks and GO and KEGG enrichment analysis

The final targets for HL, gut microbiota metabolites, and HSYA were intersected to identify common targets. These overlapping targets were then submitted to the STRING database, with the interaction score threshold set at a combined score greater than 0.4. Subsequently, Gene Ontology (GO) functional annotations and Kyoto Encyclopedia of Genes and Genomes (KEGG) pathway enrichment analyses were

performed using the WebGestalt database, KEGG pathway analysis was performed based on the KEGG database (http://www.kegg.jp/)[29–31]. A significance criterion of post-P < 0.05 and false discovery rate < 0.05 was applied, and the results were visualized using a bioinformatics platform.

Drug Evaluation and toxicity

The pharmacokinetic and toxicity profiles of metabolites associated with core genes were assessed using the SwissADME and ADMETlab platforms. High-potential candidate drug molecules were identified according to Lipinski's five rules, which stipulate that molecular weight (MW) should be less than 500 Da, hydrogen bond donors (HBD) should be fewer than 5, hydrogen bond acceptors should be fewer than 10, Moriguchi LogP (MLOGP) should be less than 4.15, Lipinski violations should be fewer than 1, the Bioavailability Score should exceed 0.1, and the topological polar surface area (TPSA) should be less than 140. These criteria were established to ensure the candidates' suitability for clinical application.

Molecular docking and molecular dynamics simulation

The molecular structures of the ligands were sourced from the PubChem database. The target protein structures, including AKT1 (PDB ID: 1UNQ), EGFR (PDB ID: 8A27), GSK3B (PDB ID: 9X2V), PPARG (PDB ID: 8BF1), RAC1 (PDB ID: 9RFF), IL6 (PDB ID: 1ALU), and TNF (PDB ID: 5UUI), were obtained from the Protein Data Bank. For receptor preparation, AutoDockTools was employed to eliminate excess macromolecules and endogenous ligands. This process was followed by the removal of water molecules, the addition of polar hydrogen atoms, and the assignment of Gasteiger charges. Subsequently, molecular docking was conducted using AutoDock 1.5.7. In the semi-flexible mode, a "genetic algorithm" search strategy was utilized to maintain receptor rigidity while allowing ligand flexibility. The optimal binding conformation and binding energy were determined and visualized using PyMOL. Batch molecular docking was carried out with AutoDock Vina, applying the widely accepted binding threshold of -5 kcal/mol to define effective ligand-receptor interactions. Molecular dynamics simulations were performed using GROMACS 2022 software. Proteins, modeled with the AMBER14SB force field, and ligands, represented by the GAFF force field, were embedded in a TIP3P water box under periodic boundary conditions to create a complex system. The system underwent initial energy minimization, followed by equilibration for 100 ps under both NVT and NPT ensembles. Subsequently, a production simulation lasting 100 ns was executed, utilizing an integration step size of 2 fs. Long-range electrostatic interactions were addressed using the particle mesh Ewald method, with a cutoff radius of 1.2 nm. Temperature (298 K) and pressure (1 bar) were maintained using the V-rescale and Berendsen algorithms, respectively. Trajectories were recorded every 10 ps and analyzed using VMD and PyMOL. The overall stability and local flexibility of the system were assessed by calculating the root mean square deviation (RMSD) of the protein-ligand complex and the root mean square fluctuation (RMSF) of individual residues. Additionally, the "Simulated Interaction Map" tool in Maestro was employed to track dynamic changes in hydrogen bonds, hydrophobic interactions, and ionic bonds between ligands and key residues throughout the simulation, thereby providing atomic-scale insights into the binding mechanism and confirming binding stability.

Statistical analysis

All tests were independently repeated a minimum of three times. Data are presented as mean ± standard deviation. Statistical analyses were conducted using GraphPad Prism 10.1.2 software. For data that satisfied normality conditions, one-way ANOVA was employed to assess the significance of the results. When the normality assumption was not met, data were reported as the median and interquartile range, and the Kruskal-Wallis test was utilized for intergroup comparisons, with $P < 0.05$ considered statistically significant. All animals were included unless otherwise specified.

Results

HSYA improved HFD-induced metabolic disturbances in mice

In this study, HFD was employed to establish a HL mouse model. The chemical structure of HSYA is illustrated in Fig. 1A. The design of the animal experiment is outlined in Fig. 1B. Throughout the experiment, the condition of the mice was monitored daily. Compared to NC, mice subjected to the HFD exhibited a glossy coat and displayed signs of obesity. Furthermore, the weight gain in the MC was significantly greater Fig. 1C, and the IPGTT levels recorded after the final administration were markedly elevated compared to NC. After four weeks of treatment, the weight gain rate in the low- and high-dose groups decreased significantly, and the rise in IPGTT levels was notably diminished Fig. 1D. Additionally, we assessed the food and water intake of mice in each group every three days. The results indicated no statistically significant differences in water intake among the groups. However, the HFD consumption in the treatment group was higher than that in the model group, suggesting that the observed inhibitory effect on weight gain in the HSYA group was not attributable to a reduction in HFD intake Fig. 1E-F. Prior to sampling, we recorded the body weights of mice in each group. The body weight of the model group was significantly greater than that of NC, while the weight gain in each administration group was controlled to a certain extent Fig. 2B. Additionally, we assessed serum glucose levels, as well as liver function indicators and renal function indicators. As illustrated in Fig. 1G-M, HFD feeding markedly elevated GLU levels in the MC of mice, adversely affecting their liver and kidney functions. Compared to the NC, the serum levels of ALT, AST, Urea, CREA, and UA in the MC group all exhibited significant increases, whereas HSYA treatment effectively mitigated these changes.

HSYA alleviated hepatic steatosis, oxidative stress, and inflammatory responses in HFD-fed mice

Upon examining the liver surface of the model group mice, mild fatty liver-like lesions were evident in some individuals, as illustrated in Fig. 2A. The liver index was significantly lower than that of the model group (Fig. 2C-D). Histopathological analysis revealed that oil red O staining of the liver indicated that HSYA treatment markedly reduced lipid deposition and improved hepatic steatosis in HL mice in a dose-dependent manner (Fig. 2A). Gross examination and H&E staining of epididymal fat demonstrated that, compared to the control group, the fat length and area in the model group mice were larger, with adipocytes appearing enlarged, dense, round, and irregularly shaped. In contrast, adipocytes in the

treatment group exhibited reduced volume and density relative to those in the model group (Fig. 2G), and both fat weight and index were effectively regulated (Fig. 2E-F). In comparison to the control group, the serum levels of TC and LDL-C in the model group of mice were significantly elevated. Treatment with high-dose HSYA and ATV markedly reduced the levels of TC and LDL-C in the model group. Although TG levels showed a decreasing trend after HSYA treatment, no statistical significance was observed. Additionally, the HDL-C levels in the model group were lower than those in the control group. Following treatment with HSYA and ATV, the HDL-C levels increased significantly, although this change also lacked statistical significance (Fig. 2H-K). These findings suggest that HFD induces disorders in lipid metabolism, resulting in hepatic fat accumulation and the potential development of fatty liver disease. HSYA effectively mitigates liver lipid accumulation, alleviates liver and epididymal steatosis, and consequently improves hepatic lipid levels. In addition, carotid ultrasound suggested a trend toward improved vascular structural parameters following HSYA treatment (Fig. S1).

Compared to the control group, serum levels of IL-6 and TNF-α were significantly elevated in mice fed HFD (Fig. 3B-C). Following HSYA intervention, the serum levels of inflammatory factors IL-6 and TNF-α, as well as the protein expression levels of IL-6, IL-1β, and TNF-α in the liver, decreased significantly (Fig. 3D-E). These findings indicate that HSYA effectively inhibits inflammatory responses. Additionally, HFD feeding significantly increased liver MDA levels and decreased SOD activity (Fig. 3E-F), suggesting that HFD induces oxidative stress and diminishes antioxidant activity. HSYA treatment reversed these alterations in a dose-dependent manner. Furthermore, the protein expression levels of HIF-1α and iNOS in the liver of the HFD group were significantly elevated (Fig. 3G-I), indicating that HFD may enhance iNOS expression through the activation of the HIF-1α signaling pathway, thereby mediating oxidative stress injury. Moreover, HFD feeding resulted in a significant increase in serum LPS levels in mice, suggesting potential impairment of intestinal barrier integrity (Fig. 3A). HSYA treatment reversed this change, potentially by modulating the structure of the intestinal microbiota and enhancing intestinal barrier function.

HSYA was associated with partial restoration of gut microbiota dysbiosis and intestinal barrier-related protein expression

Numerous studies indicate a bidirectional interaction between the host's metabolic state and the metabolism of intestinal microbiota. The observed reduction in serum LPS levels following HSYA administration suggests a potential link between its protective effects and the amelioration of intestinal dysbiosis and barrier dysfunction. To investigate the underlying mechanisms influencing serum LPS alterations, this study performed sequencing analysis targeting the V3-v4 hypervariable region of the 16S rRNA gene in the intestinal microbiota. Figure 4A displays Venn diagrams representing different groups, revealing a total of 210 operational taxonomic units (OTUs). The NC and HSYA groups harbored specific OTUs (442 and 270, respectively), while the MC group possesses 151 specific OTUs. These findings suggest that HL can alter OTU numbers compared to the normal mouse group. Analysis of α-diversity indicates that the Shannon index of the MC group is lower than that of the HSYA group. Despite lacking

statistical significance, this implies increased microbiota evenness following HSYA treatment, hinting at microbiota optimization. Additionally, the Shannon dilution curve gradually plateaus with increasing sequencing depth, indicating adequate depth for reflecting true diversity characteristics of intestinal flora in each group (Fig. 4B-C). NMDS analysis using weighted unique fraction measure (Unifrac) distances revealed distinct separation of intestinal microbiota among the three groups, with each group forming distinct microbial community clusters. This observation indicates that HL has a profound impact on the overall composition of intestinal microbiota in mice. Interventions with HSYA were found to partially modulate the composition and diversity of intestinal flora in hyperlipidemic mice, showing a beneficial effect on flora imbalance (Fig. 4D).

Further analysis of species composition indicated that HSYA significantly regulated the intestinal flora composition in hyperlipidemic mice (Fig. 4E). At the phylum level, Bacillota and Bacteroidota are closely associated with obesity and lipid metabolism disorders. Consistent with prior research, Bacillota's relative abundance increased, and Bacteroidota's decreased in the MC group compared to the NC group, leading to a notable rise in the F/B ratio. Following HSYA intervention, Bacillota decreased, and Bacteroidota rebounded. Consequently, the F/B ratio decreased, approaching normal levels, although this reduction was not statistically significant. Moreover, the MC group exhibited a significant decrease in Actinomycetota compared to the NC group, suggesting a deficiency of beneficial Actinomycetota and an imbalance in intestinal flora in HL model mice. Subsequent to HSYA intervention, the abundance of Actinomycetota and its core functional family markedly increased compared to the MC group, approaching levels observed in the normal group, indicating HSYA's capability to restore beneficial Actinomycetota abundance. At a lower taxonomic level, HSYA exerts regulatory effects on various predominant microbial groups associated with metabolic balance and intestinal barrier integrity. Genus-level analysis revealed that HSYA treatment could enhance the prevalence of Verrucomicrobiota-associated microbiota, with Akkermansia muciniphila being the principal genus representative[32], was more significantly enriched in the administration group. It is suggesting a potential association with intestinal barrier improvement. At the family level, the abundance of Muribaculaceae in the MC group was significantly decreased. As a core family within the phylum Bacteroidota, Muribaculaceae is involved in carbohydrate fermentation and intestinal barrier maintenance. Following HSYA intervention, the relative abundance of Muribaculaceae increased significantly, which may help restore intestinal microbiota homeostasis and improve metabolic disorders. Similarly, Prevotellaceae, an important functional group involved in the degradation of complex carbohydrates, production of SCFAs, and regulation of glycolipid metabolism, also exhibited a decreasing trend in the MC group. After HSYA treatment, its abundance markedly increased, approaching the level of the NC group, suggesting a potential association with metabolic regulation (Fig. 4F). Ligilactobacillus (formerly known as Lactobacillus), one of the core probiotic genus in the gut, is widely involved in host lipid metabolism, intestinal barrier maintenance, and microecological regulation. Its abundance in the HSYA group was significantly higher than that in the MC group. Unclassified_Muribaculaceae, as a core functional group of Muribaculaceae, was also significantly reduced in the MC group, while its relative abundance increased markedly after HSYA intervention (Fig. 4G). These findings suggest that HSYA may be

associated with ameliorating HL-related phenotypes by restoring key microbiota associated with complex carbohydrate metabolism, SCFA production, and lipid metabolism regulation.

Using a LDA score threshold of 4, we applied LEfSe (Fig. 4I-J). Predictions about the functional characteristics of the microbial community were made using the unobserved state reconstruction method in the community PICRUSt2 analysis. Significant differences in the metabolic potential of the intestinal microbiota were observed among the three groups of mice. Hierarchical cluster analysis, as depicted in Fig. 4H, revealed a distinct microbiota functional spectrum in the HSYA group compared to the normal NC and the MC, indicating that HSYA intervention can markedly alter the functional pathways associated with the intestinal microbiota. Notably, the modified microbial functional pathways post-HSYA treatment were notably enriched in nucleotide metabolism, encompassing de novo biosynthesis of guanylate and adenylate, synthesis of 5-aminoimidazole ribonucleotides, and the pyrimidine base salvage synthesis pathway. Furthermore, the glycolytic III pathway, L-lysine biosynthesis, and UDP-N-acetylmuramyl pentapeptide biosynthesis pathway exhibited relatively higher enrichment in the HSYA group. These findings suggest that HSYA can partially reconfigure the metabolic potential of the intestinal microbiota, particularly by modulating pathways related to nucleotide synthesis, carbohydrate metabolism, amino acid biosynthesis, and bacterial structural metabolism, which may underlie its therapeutic effects.

In response, we conducted additional analysis on the expression levels of tight junction proteins ZO-1 and Occludin in colon tissue. The findings revealed a significant decrease in the expressions of ZO-1 and Occludin in the MC group compared to the NC group. However, following HSYA intervention, both expressions notably recovered (Fig. 4K-L). This indicates that HSYA may partially mitigate HFD-induced intestinal barrier damage, aligning with its ability to lower serum LPS levels.

Integrated network pharmacology and gutMGene predicted lipid metabolism- and inflammation-related pathways underlying the effects of HSYA

The results indicate that HSYA can enhance the structure of the intestinal microbiota, decrease serum LPS levels, and restore the expression of colonic tight junction proteins. From the gutMGene v2.0 database, 613 gut microbiota metabolites were extracted, with 167 metabolites having structural information available in SMILES format via the SEA and STP platforms. By intersecting the predicted 167 metabolites, 610 common targets were revealed as the potential targets of gut microbiota metabolites. Furthermore, 3,449 targets linked to HL were identified from the GeneCards, DisGeNET, and OMIM databases. Additionally, 452 targets were acquired for HSYA from the TCMSP and STP databases, with 212 target genes identified after overlapping with diseases. Through the intersection of these targets with 610 intestinal microbiota metabolite targets and intestinal-related genes, 15 final overlapping targets were obtained, Hub targets were identified based on degree centrality using the CytoHubba plugin in Cytoscape. (Fig. 5A-D). A network diagram illustrating the interplay of gut microbiota, targets, and HL, along with PPI analysis, was created to depict the regulatory connections (Fig. 5E-F). GO enrichment analysis unveiled that pertinent pathways were enriched in biological processes such as

reactive oxygen species metabolism, and responses to oxidative stress, as well as molecular functions like protein serine/threonine kinase activity (Fig. 5G). The KEGG outcomes indicated significant enrichment in lipid metabolism and conditions like atherosclerosis, non-alcoholic fatty liver disease, and insulin resistance, as well as pathways including PI3K-AKT, HIF-1, TNF, and others (Fig. 5H). Additionally, a "microbiota-substrate-metabolite-target" network was established to visualize the intricate interactions, showcasing the relationships among intestinal microbiota, metabolic substrates, metabolites, and targets (Fig. 5I). To ensure the safety of docking therapy for key metabolites, a toxicity characteristic analysis was conducted. SwissADME analysis revealed that several compounds, such as Phenylacetylglutamine, (Z)-10-hydroxyoctadec-12-enoic acid, and Histidine, adhere to Lipinski's five rules. ADMETlab analysis confirmed favorable drug similarity (Table 2). The gut microbiota metabolites assessed showed low to moderate risk levels concerning carcinogenicity, hERG inhibition, human hepatotoxicity (H-HT), drug-induced liver injury (DILI), and oral LD50 (Table 3, Table S2). These findings suggest that the chosen substrate exhibits acceptable toxic properties. While further validation is necessary, it holds promise for the clinical application of HSYA.

Table 2
The evaluation of toxicity on key metabolites

Compound	MW	HBA	HBD	MLOGP	Lipinski violations	Bioavailability Score	TPSA
Phenylacetylglutamine	264.28	4	3	0.4	0	0.56	109.49
1-(3-Chloro-2,6-dihydroxy-4-methoxyphenyl)-1-hexanone	272.72	4	2	1.92	0	0.55	66.76
Butyrate	87.1	2	0	0.49	0	0.85	40.13
Propionate	73.07	2	0	0.03	0	0.85	40.13
Valeric acid	102.13	2	1	0.89	0	0.85	37.3
Isovaleric acid	102.13	2	1	0.89	0	0.85	37.3
10-keto-12Z-octadecenoic acid	296.44	3	1	3.59	0	0.85	54.37
(Z)-10-hydroxyoctadec-12-enoic acid	298.46	3	2	3.69	0	0.85	57.53
Succinate	116.07	4	0	-0.54	0	0.56	80.26
Histidine	155.15	4	3	-3.74	0	0.55	92

Lipinski's rule of five: MW < 500; HBA < 10; HBD ≤ 5; MLOGP ≤ 4.15; Lipinski violations ≤ 1; bioavailability score > 0.1; TPSA < 140.

Table 3
The evaluation of toxicity on key metabolites.

Compound	hERG	H-HT	DILI	Carcinogenicity	LD50_oral
Phenylacetylglutamine	0.026	0.361	0.374	0.237	0
1-(3-Chloro-2,6-dihydroxy-4-methoxyphenyl)-1-hexanone	0.131	0.453	0.262	0.338	0
Butyrate	0.025	0.327	0.248	0.398	0
Propionate	0.029	0.348	0.317	0.447	0
Valeric acid	0.030	0.326	0.227	0.382	0
Isovaleric acid	0.029	0.403	0.253	0.484	0
10-keto-12Z-octadecenoic acid	0.098	0.211	0.008	0.062	0
(Z)-10-hydroxyoctadec-12-enoic acid	0.125	0.301	0.005	0.063	0
Succinate	0.004	0.363	0.289	0.358	0
Histidine	0.045	0.383	0.042	0.154	0

Molecular docking experiments were performed on the primary target using HSYA and essential metabolites. The study encompassed the anticipated key protein targets (AKT1, TNF, IL6, EGFR, GSK3B, PPARG, RAC1). The interaction strength between ligands and receptor proteins was assessed based on binding affinity, and the molecular docking score was depicted as a heat map in Fig. 6E. These results provide supportive but not definitive evidence of target engagement. Every protein underwent molecular docking analysis with each compound. Figure 6A-D illustrates the typical two-dimensional and three-dimensional structural representations of the primary metabolites exhibiting the lowest binding energy and their respective targets. These metabolites predominantly engage with the docking proteins via hydrogen bonds, π-alkyl interactions, van der Waals forces, and the establishment of enduring complexes. To assess the stability of the HSYA-AKT1 complex, we performed molecular dynamics simulations. Figure 6F illustrates a single global energy minimum in the Gibbs energy landscape, suggesting a high concentration of conformations in predominantly stable and homogeneous clusters. Free Energy Landscape (FEL) analysis (Fig. 7A) reveals distinct low-energy basins separated by energy barriers, indicating the presence of various stable conformational states of the HSYA-AKT1 complex throughout the simulation. As illustrated in Fig. 7B, the number of hydrogen bonds between HSYA and

AKT1 varies between 1 and 8, with an average of approximately 4 hydrogen bonds throughout the simulation. Notably, no complete dissociation of hydrogen bonds was observed, suggesting a persistent and stable interaction at the binding interface, and indicating that HSYA binding does not disrupt the overall structure of AKT1. The root mean square deviation (RMSD) rapidly reached equilibrium and remained relatively stable thereafter (Fig. 7D), demonstrating that HSYA binding does not induce significant structural disturbances in AKT1. Over time, the radius of gyration (Rg) remained stable (Fig. 7C), signifying that the overall density of the protein remained unchanged. Root-mean-square fluctuation (RMSF) analysis revealed limited fluctuations for most residues, while the flexibility of residues near the binding pocket decreased (Fig. 7E), indicating that HSYA binding restricted local conformational dynamics. Similarly, the solvent-accessible surface area (SASA) exhibited only minor changes, further supporting the structural stability of the complex (Fig. 7F). Energy decomposition analysis of each residue identified several key residues that significantly contributed to ligand binding, primarily located within the functional binding pocket of AKT1 (Fig. 7G). Furthermore, the total binding free energy was predominantly negative (Fig. 7H), indicating that this interaction is favorable and spontaneous.

HSYA modulated hepatic inflammatory and lipogenic signaling in vivo

To validate the key signaling pathways identified through the integrated analysis, Western blot analysis of liver samples demonstrated that HSYA modulated the expression of proteins involved in inflammation and lipid metabolism (Fig. 8A-B, Fig. 3H). Comparative analysis revealed elevated levels of p-PI3K/PI3K, p-AKT/AKT, p-NF-κB/NF-κB, HIF-1α, and SREBP-1c in the liver tissues of the MC group compared to the NC group, indicating activation of pathways associated with liver inflammation and lipid biosynthesis under hyperlipidemic conditions. Following HSYA intervention, a significant decrease in the levels of p-PI3K/PI3K, p-AKT/AKT, p-NF-κB/NF-κB, HIF-1α, and SREBP-1c in liver tissue was observed relative to the MC group, suggesting that HSYA can modulate aberrant signaling linked to liver inflammation and lipid biosynthesis in vivo, thereby ameliorating liver damage induced by HL.

HSYA protected HepG2 cells against PA-induced lipotoxicity and regulated lipid metabolism-related gene expression

The aforementioned findings validated the hepatoprotective efficacy of HSYA in HFD-induced mice. Subsequently, HepG2 cells were cultured in vitro to delve deeper into its protective mechanisms. The CCK8 assay was employed to assess the viability of HepG2 cells (0-320 μM) following a 24-hour exposure to HSYA. It was observed that varying concentrations of HSYA did not significantly impact cell viability compared to the control group (Fig. 9A), thus confirming the non-toxic nature of HSYA towards HepG2 cells within the 80–320 μM range, facilitating its utilization in subsequent experiments. Furthermore, exposure of HepG2 cells to PA (0–1 mM) for 24 hours resulted in a dose-dependent reduction in cell viability. At a PA concentration of 0.5 mM, the relative survival rate was approximately

50% of the control group. Hence, 0.5 mM PA was chosen as the optimal concentration for modeling and subsequent investigations (Fig. 9B). HepG2 cells were exposed to 0.5 mM PA per well, followed by the introduction of HSYA (1.25, 2.5, 5, 10, 20, 40, 80, 160, 320, 640 μM) after a 24-hour incubation period. Subsequently, cell viability was assessed using the CCK-8 assay after another 24 hours. The cell viability of the PA treatment group exhibited a significant decrease, whereas HSYA demonstrated a superior protective effect on HepG2 cells damaged by PA within the concentration range of 80–320 μM (Fig. 9C). Analysis in Fig. 9D-E revealed a significant increase in TC and TG levels in HepG2 cells induced by PA. Following drug administration, there was a notable decrease in TG and TC levels. Particularly, at a concentration of 320 μM HSYA, each parameter exhibited significant differences compared to the model group, with TG content showing the most pronounced impact. Consequently, HSYA was found to ameliorate lipid accumulation in HepG2 cells induced by PA. Furthermore, results from oil red O staining indicated that treatment with HSYA or 5 μmol/L ATV led to a reduction in lipid droplet density in HepG2 cells, thereby alleviating lipid accumulation (Fig. 9F).

We assessed the mRNA expression of lipid metabolism-related genes in HepG2 cells treated with PA using quantitative reverse transcription polymerase chain reaction (qRT-PCR). Compared to the control group, PA treatment significantly upregulated the expression of lipid production-related genes SREBP-1c and FASN, while downregulating the expression of key fatty acid β-oxidation genes Carnitine palmitoyltransferase 1A (CPT1A) and peroxisome proliferator-activated receptor α (PPARA). Following intervention with HSYA, the expressions of SREBP-1c and FASN decreased, whereas the expressions of CPT1A and PPARA increased (Fig. 9G). These results suggest that HSYA can inhibit lipid synthesis and promote fatty acid catabolism. Additionally, PA treatment significantly induced the expression of inflammation-related genes IL-6 and TNF-α, which were notably downregulated after HSYA intervention (Fig. 9H). This finding further supports the anti-inflammatory effect of HSYA in vitro.

Based on the above in vivo and in vitro results, HSYA can regulate abnormal signaling pathways related to liver inflammation and lipid production, and alleviate lipotoxic damage in HepG2 cells induced by PA. This result is consistent with the results of network pharmacology and intestinal-related analyses.

Discussion

HL, a prevalent metabolic disorder, is intricately linked to heightened lipid consumption and irregular lipid metabolism. Despite thorough investigations, the underlying pathogenesis of HL remains elusive. Present therapeutic approaches, such as statins, cholesterol absorption inhibitors, PCSK9 inhibitors, probucol, and other lipid-lowering medications, are commonly employed; however, they are constrained by inherent limitations and adverse effects[3,33]. Identifying therapeutic targets and developing additional drug interventions are critical to optimizing the management of HL. This study presents evidence that the natural compound HSYA, derived from Carthamus tinctorius L., attenuates hepatic inflammation and improves intestinal barrier function by targeting the PI3K/AKT/HIF-1α axis, accompanied by modulation of NF-κB signaling, thereby alleviating HL.

Consistent with previous studies[34], mice fed a 60% high-fat diet exhibited pronounced metabolic disturbances, such as abnormal weight increase, impaired glucose tolerance, liver steatosis, hepatocellular injury, and systemic metabolic irregularities. These alterations were validated through phenotypic, biochemical, and pathological assessments. HSYA treatment markedly ameliorated these deviations compared to the MC group. The accumulation of TG and the onset of HL result from excessive consumption of exogenous fatty acids or excessive endogenous fatty acid synthesis in liver cells[35]. SREBP-1c and FASN proteins play a key role in the synthesis of endogenous fatty acids. HSYA can significantly down-regulate the expression levels of these proteins and mrnas, thereby inhibiting the synthesis of endogenous fatty acids and reducing the accumulation of TG, and thus delaying the progression of HL. In addition, the upregulation of PPARA and CPT1A proteins in the liver by HSYA leads to an enhanced oxidation of β -fatty acids, thereby promoting a reduction in intracellular lipid content.

Research on HL increasingly highlights the role of the intestinal microbiota and intestinal barrier function, as their dysregulation constitutes a fundamental mechanism underlying the onset and progression of the disease. The intestinal epithelial barrier and microbiota may represent potential new pharmacological targets for HSYA. In healthy individuals, the two most abundant bacterial phyla in the intestinal tract—Bacillota and Bacteroidota—maintain a relative balance[36]. In this study, gut microbiota detection revealed that the composition of certain specific bacterial genera in HFD-stimulated mice changed significantly after HSY treatment, suggesting that HSYA has a positive effect on the coordinated improvement of the microbiota and the host's overall metabolic state. However, in untreated HFD-stimulated mice, microbiota dysbiosis leads to an imbalance in the F/B ratio. The numbers of beneficial bacteria (such as Akkermansia muciniphila, Verrucomicrobiota and Muribaculaceae) and bacteria that produce SCFAs decreased significantly; Conversely, the abundance of bacteria secreting LPS in the intestinal tract significantly increased. The abundance of Romboutsia, a pro-inflammatory bacterium that may damage the intestinal barrier, was notably enhanced. Its abundance is closely related to blood lipid levels and the degree of nonalcoholic fatty liver disease[37]. If LPS enters systemic circulation, it can promote the absorption and production of FFAs by the liver, cause liver inflammation and HL[38,39], and may increase the risk of coronary heart disease[40]. In the HSYA group, there was a significant reduction in the abundance of Romboutsia, leading to a decrease in serum LPS levels, thereby slowing down the progression of LPS-aggravated HL. The disruption of gut microbiota balance can compromise intestinal tight junction integrity. HSYA mitigates intestinal permeability by enhancing the protein expression of intestinal tight junction proteins ZO-1 and Occludin, thereby restoring the intestinal barrier function.

The PI3K/AKT pathway plays a context-dependent role in metabolic regulation. While physiological activation of AKT contributes to lipid homeostasis, sustained or aberrant activation under hyperlipidemic conditions has been reported to promote lipogenesis, inflammatory responses, and hepatic steatosis[41]. Excessive circulating lipids, especially free fatty acids, can accumulate ectopic in liver cells and other peripheral tissues, thereby causing lipid toxicity, mitochondrial dysfunction and impaired cellular respiration[42]. This process is often accompanied by excessive generation of reactive oxygen species,

which not only aggravates oxidative damage but also activates inflammatory signaling pathways such as NF-κB and their downstream mediators[22,43]. Under the background of HFD, HIF-1α promotes lipid synthesis by inhibiting mitochondrial oxidative phosphorylation, thereby aggravating liver lipid toxicity[44]. These pathways converge into an interrelated network of inflammation, metabolism and hypoxia, providing multi-dimensional therapeutic entry points[45]. Based on this, we speculate that drugs or compounds exhibiting antioxidant and anti-inflammatory properties may synergistically address HL through various target organs. By integrating gutMGene v2.0 with network pharmacology analysis, along with the five rules of Lipinski drugs and computer toxicology predictions, this study identified 10 key metabolites as preferred intervention targets. Among these pathways, the PI3K/AKT/HIF-1α axis appears to play a central role. Notably, molecular docking and molecular dynamics simulations confirmed that HSYA is a high-affinity binder of AKT1, positioning it may interact with AKT1, potentially modulating its activity. These findings underscore the pivotal role of AKT1 as a primary regulator and drug target in HL. Furthermore, HSYA significantly improved oxidative stress levels, reduced the concentration of related inflammatory factors in serum, and decreased the expression levels of their proteins and mRNAs. This suggests that HSYA may contribute to delaying the progression of chronic inflammation associated with HL, potentially linked to the dual role of HIF-1 across different organs and disease contexts.

Traditional Chinese Medicine has shown good therapeutic effects in the long-term treatment of HL[46]. A variety of natural small molecules have diverse pharmacological effects and can simultaneously regulate multiple pathological targets. HSYA has antioxidant, anti-inflammatory and metabolic regulatory effects[26,47]. In this investigation, we established a HL mouse model induced by HFD and a lipotoxicity model in HepG2 cells induced by PA. We elucidated the coordinated regulation of lipid metabolism and intestinal barrier function primarily through modulation of the PI3K/AKT/HIF-1α signaling pathway, accompanied by regulation of NF-κB signaling and gut microbiota. However, the causal role of PI3K/AKT signaling requires further validation using pathway-specific inhibitors. The specific mechanisms underlying the interaction between HSYA and AKT1, particularly its effects on lipid metabolism and pathways related to microbiota metabolites, warrant further exploration through non-targeted or targeted metabolomics to identify the microbial products responsible for the protective effects of HSYA. Subsequent investigations could involve fecal microbiota transplantation, pathogen-specific interventions, or metabolite supplementation to more precisely elucidate these mechanisms. Furthermore, a more comprehensive characterization of the pharmacokinetic profile of HSYA is essential. A limitation of this study is the use of only male mice, which hinders the verification of HSYA's applicability to female populations. Future experiments will address this limitation by examining the efficacy of HSYA in improving HL in female mice to elucidate potential gender-specific responses.

Conclusions

In the present study, both in vivo and in vitro experiments confirmed that HSYA can alleviate HFD-induced HL by regulating the PI3K/AKT/HIF-1α signaling pathway and improving the homeostasis of

host gut microbiota. The results demonstrated that HSYA effectively attenuated the inflammatory response induced by lipid accumulation. Meanwhile, it enhanced the body's antioxidant defense capacity, thereby ameliorating lipid metabolism disorders. Furthermore, network pharmacology analysis and cytotoxicity assays revealed that HSYA exhibited low cytotoxicity and favorable safety profiles, providing important safety support for its subsequent drug development and clinical application. Therefore, based on the comprehensive results of in vivo and in vitro experiments as well as safety evaluations, HSYA may serve as a potential candidate for the treatment of hyperlipidemia. This study not only elucidated its molecular mechanisms underlying lipid-lowering effects, but also laid a solid theoretical foundation for the subsequent research and development, dosage form optimization, and clinical translation of HSYA. Future studies may further explore the specific mechanisms by which HSYA exerts anti-hyperlipidemic effects via coordinating gut microbiota and regulating intestinal barrier function, and provide more sufficient experimental evidence to promote the clinical translation and application of HSYA.

Abbreviations

HL	Hyperlipidemia
HSYA	Hydroxysafflor yellow A
ATV	atorvastatin
AST	aspartate transaminase
ALT	alanine transaminase
TC	total cholesterol
TG	triglycerides
LDL-C	low-density lipoprotein cholesterol
HDL-C	high-density lipoprotein cholesterol
HFD	high-fat diet
NFD	normal-fat diet
GSK-3B	glycogen synthase kinase-3β
SREBP-1c	sterol regulatory element-binding protein-1c
PPARG	peroxisome proliferator-activated receptor γ
PPARA	peroxisome proliferator-activated receptor α
LPS	lipopolysaccharide
CPT1A	Carnitine palmitoyltransferase 1A
PA	palmitic acid
ZO-1	Zonula occludens-1
PPI	Protein–protein interaction
PHDs	prolyl hydroxylases
OTUs	operational taxonomic units
NMDS	non-metric multidimensional scaling analysis
LEfSe	Linear discriminant analysis effect size
PICRUSt2	phylogenetic Study 2
GO	Gene Ontology
KEGG	Encyclopedia of Genes and Genomes
MW	molecular weight
HBD	hydrogen bond donors

MLOGP	Moriguchi LogP
TPSA	topological polar surface area
RMSD	root mean square deviation
RMSF	root-mean-square fluctuation
FEL	Free energy landscape
SASA	solvent-accessible surface area
SCFAs	short-chain fatty acids

Declarations

Author contributions

Caiyou Xu and Keman Ji have contributed equally to this work and share first authorship. Conceptualization, Caiyou Xu and Keman Ji; Data curation, Caiyou Xu, Haoran Li and Yan Sun; Formal analysis, Caiyou Xu, Jiabo Zhang and Keman Ji; Funding acquisition, Caiyou Xu, Manping Wu, Keman Ji and Chunling Liu; Investigation, Caiyou Xu and Keman Ji; Methodology, Caiyou Xu, Manping Wu and Keman Ji; Project administration, Caiyou Xu, and Chunling Liu; Software, Caiyou Xu and Jiabo Zhang; Supervision, Chao Chen, Chunling Liu; Validation, Chunling Liu; Visualization, Caiyou Xu and Jiabo Zhang; Writing – original draft, Caiyou Xu; Writing – review & editing, Caiyou Xu, Keman Ji, Ruge Niu and Jiabo Zhang.

Funding

This study is supported by the Jiangsu Provincial Postgraduate Research & Practice Innovation Program (Grant No. KYCX25_2314).

Acknowledgements

We thank the Central Laboratory of Nanjing University of Chinese Medicine for its help and guidance during the entire experiment.

Data and materials availability

The 16S rRNA sequencing data generated in this study are publicly available in the NCBI Sequence Read Archive (SRA) under the BioProject accession PRJNA1466257. The data are scheduled to be released on August 1, 2026, and will be accessible at https://www.ncbi.nlm.nih.gov/sra/PRJNA1466257. All other data and materials supporting this study are available from the corresponding author upon reasonable request.

Ethics approval and consent to participate

All animal experimental procedures were performed in accordance with the protocol approved by the Animal Ethics Committee in Affiliated Hospital of Nanjing University of Traditional Chinese Medicine (No. 2025DW-063-01). The study did not involve human participants, human data, or human tissue.

Competing interests

The authors declare no competing interests.

References

1. Wiggins, B. S. et al. Dyslipidemia Guideline-at-a-Glance. *J Am Coll Cardiol* (2026). (2026).
2. Pirillo, A., Casula, M., Olmastroni, E., Norata, G. D. & Catapano, A. L. Global epidemiology of dyslipidaemias. *Nat. Rev. Cardiol.* **18**, 689–700 (2021).
3. Zeng, W. et al. Advances in statin adverse reactions and the potential mechanisms: A systematic review. *J. Adv. Res.* **76**, 781–797 (2025).
4. Manning, B. D. & Cantley, L. C. AKT/PKB signaling: navigating downstream. *Cell* **129**, 1261–1274 (2007).
5. Lai, P. et al. SR-A3 suppresses AKT activation to protect against MAFLD by inhibiting XIAP-mediated PTEN degradation. *Nat. Commun.* **16**, 2430 (2025).
6. Wu, Z. et al. Improvement of obesity by Liupao tea is through the IRS-1/PI3K/AKT/GLUT4 signaling pathway according to network pharmacology and experimental verification. *Phytomedicine* **110**, 154633 (2023).
7. Wu, D. et al. Celastrol Alleviates Intestinal Epithelial Permeability by Inhibiting Ferroptosis through PI3K/Akt/FOXO1/HO-1 Signaling Pathway. *Am. J. Chin. Med.* **53**, 1207–1224 (2025).
8. Bakirtzi, K. et al. The neurotensin-HIF-1α-VEGFα axis orchestrates hypoxia, colonic inflammation, and intestinal angiogenesis. *Am. J. Pathol.* **184**, 3405–3414 (2014).
9. Manalo, D. J. et al. Transcriptional regulation of vascular endothelial cell responses to hypoxia by HIF-1. *Blood* **105**, 659–669 (2005).
10. Semenza, G. L. Regulation of cancer cell metabolism by hypoxia-inducible factor 1. *Semin Cancer Biol.* **19**, 12–16 (2009).
11. Wang, Y. et al. Glycolysis and beyond in glucose metabolism: exploring pulmonary fibrosis at the metabolic crossroads. *Front. Endocrinol. (Lausanne)*. **15**, 1379521 (2024).
12. Tannahill, G. M. et al. Succinate is an inflammatory signal that induces IL-1β through HIF-1α. *Nature* **496**, 238–242 (2013).
13. Ivan, M. et al. HIFalpha targeted for VHL-mediated destruction by proline hydroxylation: implications for O2 sensing. *Science* **292**, 464–468 (2001).
14. Ting, K. K. Y. et al. Cholesterol accumulation impairs HIF-1α-dependent immunometabolic reprogramming of LPS-stimulated macrophages by upregulating the NRF2 pathway. *Sci. Rep.* **14**, 11162 (2024).

15. Semenza, G. L. Hypoxia-inducible factor 1 and cardiovascular disease. *Annu. Rev. Physiol.* **76**, 39–56 (2014).
16. Zhong, Y. et al. Advances in understanding the role of gut microbiota in fat deposition and lipid metabolism. *J. Anim. Sci. Biotechnol.* **16**, 152 (2025).
17. Pral, L. P., Fachi, J. L., Corrêa, R. O., Colonna, M. & Vinolo, M. A. R. Hypoxia and HIF-1 as key regulators of gut microbiota and host interactions. *Trends Immunol.* **42**, 604–621 (2021).
18. Ma, S., Yeom, J. & Lim, Y. H. Specific activation of hypoxia-inducible factor-2α by propionate metabolism via a β-oxidation-like pathway stimulates MUC2 production in intestinal goblet cells. *Biomed. Pharmacother*. **155**, 113672 (2022).
19. Chen, H. et al. The Potential Role of Hypoxia-Inducible Factor-1 in the Progression and Therapy of Central Nervous System Diseases. *Curr. Neuropharmacol.* **20**, 1651–1666 (2022).
20. Xiong, L. et al. Acute exposure to high-fat diet impairs ILC3 functions and gut homeostasis. *Immunity* **58**, 1185–1200e1188 (2025).
21. Yan, F. et al. Glycoside combinations of Buyang Huanwu decoction ameliorate atherosclerosis via STAT3, HIF-1, and VEGF. *Naunyn Schmiedebergs Arch. Pharmacol.* **396**, 1187–1203 (2023).
22. Liang, N. et al. Fatty acid oxidation-induced HIF-1α activation facilitates hepatic urate synthesis through upregulating NT5C2 and XDH. *Life Metab.* **3**, loae018 (2024).
23. Yang, Y. et al. Hydroxy Safflower Yellow A: A Natural Compound from Carthamus tinctorius L. with Potent Activity Against Liver Fibrosis and Cancer. *Phytomedicine* **153**, 157858 (2026).
24. Wu, X. et al. Extraction, Structures, Bioactivities and Structure-Function Analysis of the Polysaccharides From Safflower (Carthamus tinctorius L). *Front. Pharmacol.* **12**, 767947 (2021).
25. Wang, P. et al. Network Pharmacology Combined With Gut Microbiome and Serum Metabolomics Reveals the Therapeutic Mechanisms of Hydroxysafflor Yellow A in Diabetic Kidney Disease. *J Diabetes Res* e2131566 (2026). (2026).
26. Wang, W. et al. Hydroxysafflor yellow A ameliorates alcohol-induced liver injury through PI3K/Akt and STAT3/NF-κB signaling pathways. *Phytomedicine* **132**, 155814 (2024).
27. Feng, X. et al. Hydroxysafflor yellow A regulates lymphangiogenesis and inflammation via the inhibition of PI3K on regulating AKT/mTOR and NF-κB pathway in macrophages to reduce atherosclerosis in ApoE-/- mice. *Phytomedicine* **112**, 154684 (2023).
28. Percie du Sert. Reporting animal research: Explanation and elaboration for the ARRIVE guidelines 2.0. *PLoS Biol.* **18**, e3000411 (2020).
29. Kanehisa, M., Furumichi, M., Sato, Y., Matsuura, Y. & Ishiguro-Watanabe, M. KEGG: biological systems database as a model of the real world. *Nucleic Acids Res.* **53**, D672–d677 (2025).
30. Kanehisa, M. Toward understanding the origin and evolution of cellular organisms. *Protein Sci.* **28**, 1947–1951 (2019).
31. Ogata, H. et al. KEGG: Kyoto Encyclopedia of Genes and Genomes. *Nucleic Acids Res.* **27**, 29–34 (1999).

32. Depommier, C. et al. Supplementation with Akkermansia muciniphila in overweight and obese human volunteers: a proof-of-concept exploratory study. *Nat. Med.* **25**, 1096–1103 (2019).
33. Tsui, L., Wang, D., Fan, C. & Shi, C. A hierarchical risk assessment framework for head-to-head comparison of statin safety profiles in Chinese patients. *Sci Rep* (2026).
34. Sun, L. et al. Ablation of gut microbiota alleviates obesity-induced hepatic steatosis and glucose intolerance by modulating bile acid metabolism in hamsters. *Acta Pharm. Sin B*. **9**, 702–710 (2019).
35. Fang, X. et al. Molecular Mechanism Pathways of Natural Compounds for the Treatment of Non-Alcoholic Fatty Liver Disease. *Molecules* **28** (2023).
36. Ma, J. et al. Gut-liver axis mechanisms of Hippophae rhamnoides L. in non-alcoholic fatty liver disease prevention. *Phytomedicine* **149**, 157517 (2025).
37. Mu, H. et al. Naringin Attenuates High Fat Diet Induced Non-alcoholic Fatty Liver Disease and Gut Bacterial Dysbiosis in Mice. *Front. Microbiol.* **11**, 585066 (2020).
38. Zhang, X. Y. et al. Phlorizin ameliorates obesity-associated endotoxemia and insulin resistance in high-fat diet-fed mice by targeting the gut microbiota and intestinal barrier integrity. *Gut Microbes*. **12**, 1–18 (2020).
39. Pabst, O. et al. Gut-liver axis: barriers and functional circuits. *Nat. Rev. Gastroenterol. Hepatol.* **20**, 447–461 (2023).
40. Wang, S. et al. Gut microbiota-derived proinflammatory biomarkers and risk of coronary heart disease: a prospective study among United States males and females. *Am. J. Clin. Nutr.* **122**, 1602–1612 (2025).
41. Zhang, Y. et al. 4-Hydroxybenzyl Alcohol Mitigates Hyperlipidemia-Associated Depression by Inhibiting Neuroinflammation via the NKIRAS2/NF-κB Pathway. *Adv Sci. (Weinh)*, e17873 (2026).
42. Livshits, G. & Kalinkovich, A. Inflammaging as a common ground for the development and maintenance of sarcopenia, obesity, cardiomyopathy and dysbiosis. *Ageing Res. Rev.* **56**, 100980 (2019).
43. Alshareef, N. S., AlSedairy, S. A., Al-Harbi, L. N., Alshammari, G. M. & Yahya, M. A. Carthamus tinctorius L. (Safflower) Flower Extract Attenuates Hepatic Injury and Steatosis in a Rat Model of Type 2 Diabetes Mellitus via Nrf2-Dependent Hypoglycemic, Antioxidant, and Hypolipidemic Effects. *Antioxidants (Basel)* 13 (2024).
44. Halberg, N. et al. Hypoxia-inducible factor 1alpha induces fibrosis and insulin resistance in white adipose tissue. *Mol. Cell. Biol.* **29**, 4467–4483 (2009).
45. Aguilar, D. & Fernandez, M. L. Hypercholesterolemia induces adipose dysfunction in conditions of obesity and nonobesity. *Adv. Nutr.* **5**, 497–502 (2014).
46. Chang, J. et al. Perilla Seed Oil Alleviates High-Fat-Diet-Induced Hyperlipidemia by Regulating Fatty Acid Metabolism via the PI3K/Akt/NOS3 Pathway. *Foods* **14** (2025).
47. Wu, L. et al. Hydroxysafflor yellow A alleviates oxidative stress and inflammatory damage in the livers of mice with nonalcoholic fatty liver disease and modulates gut microbiota. *Front. Pharmacol.* **16**, 1568608 (2025).

Figures

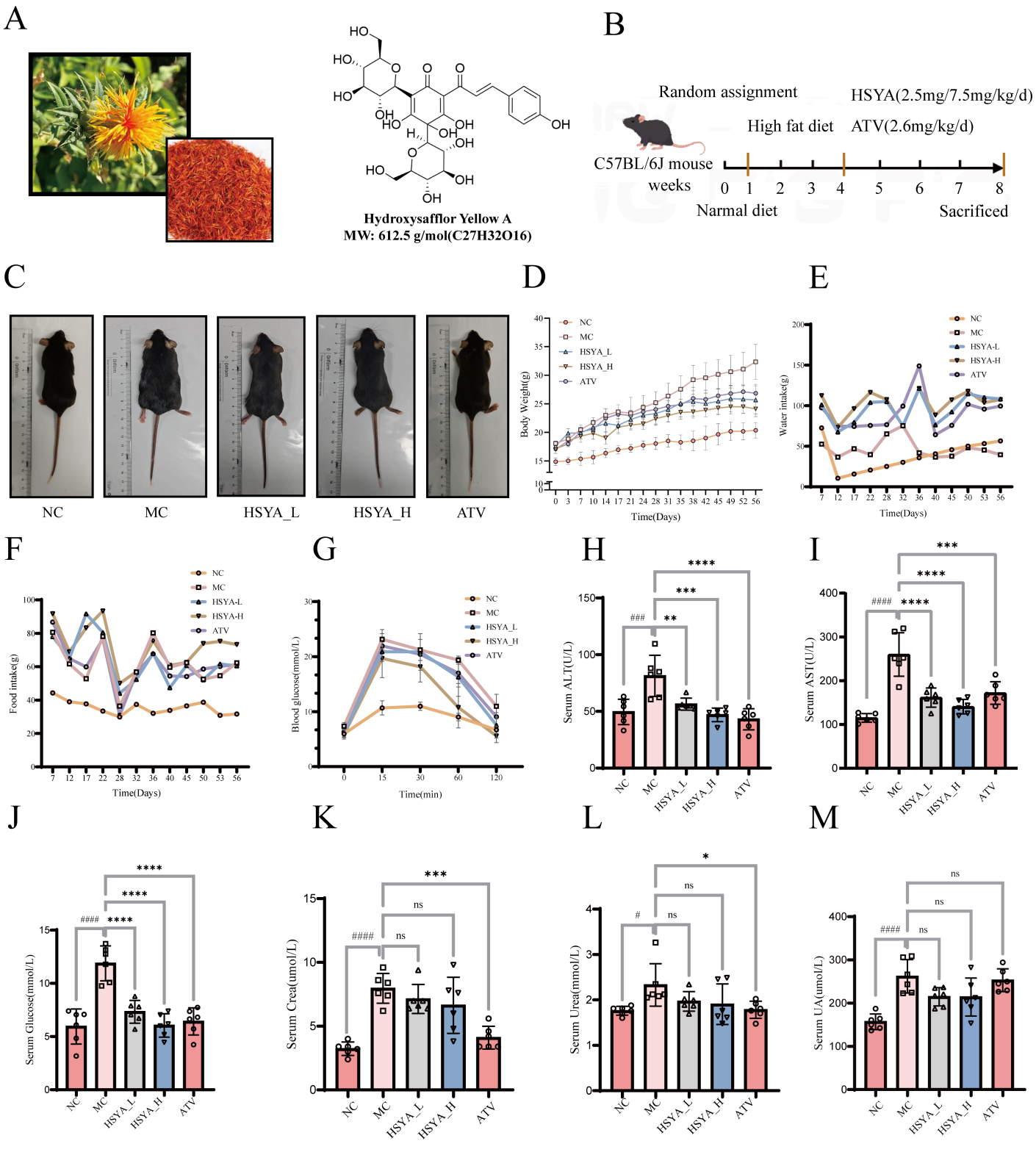


Figure 1

The alleviating effects of HSYA on weight and liver and kidney function induced by a HFD are examined. The chemical structure of HSYA is depicted in panel **A**. The experimental timeline is illustrated in panel **B**. Panels **C** and **D** present a comparison of body weight changes among the groups, while panels **E** and

F show the average food and water intake. IPGTT as shown in panel **G**. Panels **H**-**M** display serum levels of ALT, AST, GLU, creatinine, urea, and UA. Data are expressed as mean ± standard error (n=6). Statistical significance is indicated as follows: #p< 0.05, ###p < 0.001, ####p < 0.0001 vs. NC; *p< 0.05, **p < 0.005, ***p < 0.001, ****p < 0.0001 vs. MC. ns indicates P >0.05.

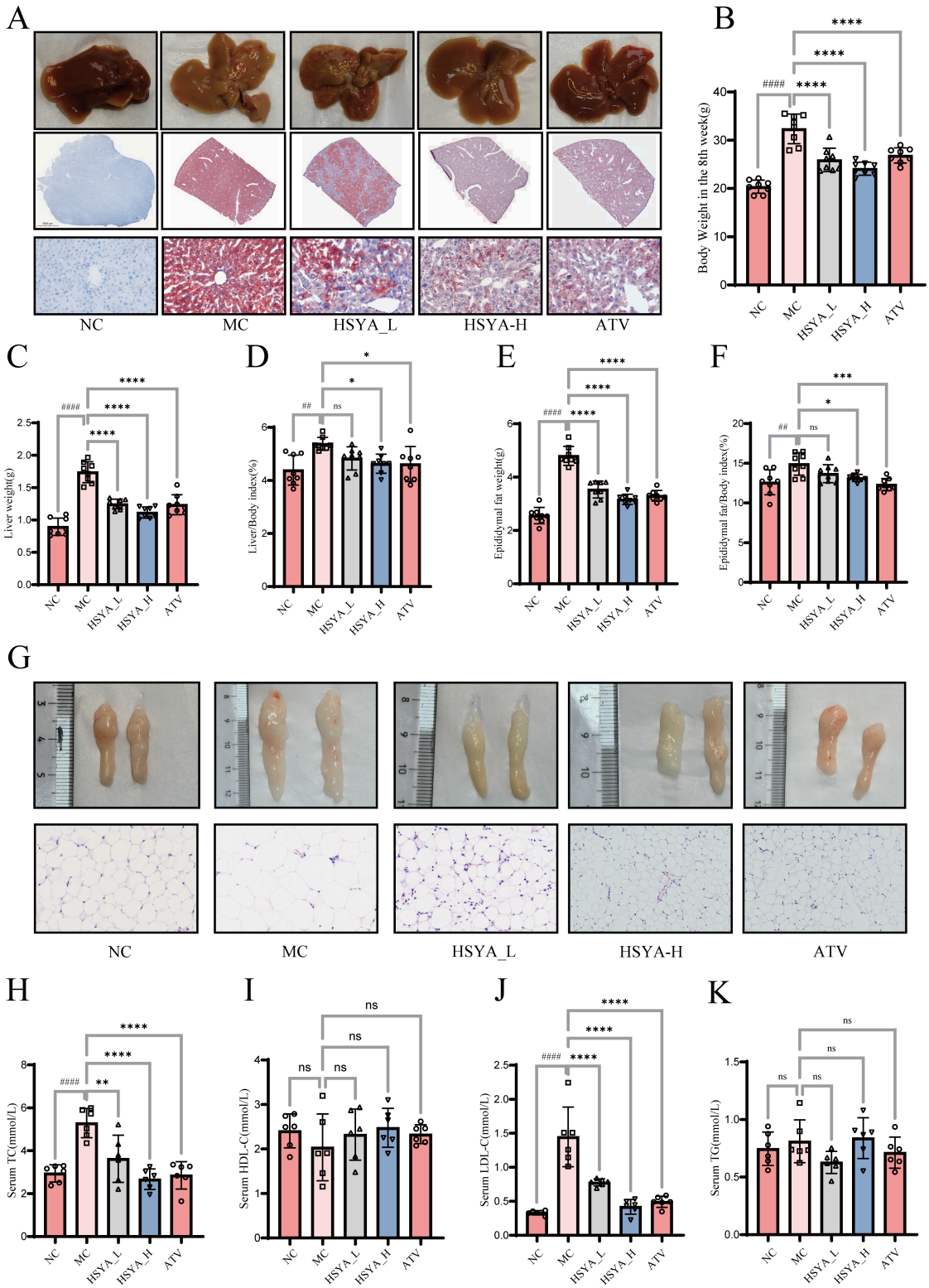


Figure 2

The influence of HSYA on the histological pathology of liver, Epididymal fat and blood lipid levels in hyperlipidemic mice. **A** liver photo and oil red staining (scale bars: 5 mm and 200 μm). **B** The body weight of mice in each group at the end of the experiment. **C-D** Liver weight and liver index, **E-F** Epididymal fat weight and Epididymal fat index. **G** Epididymal fat photo and H&E stained sections (scale bars: 5 mm and 200 μm). **H** The serum level of TC. **I** The serum level of HDL-C. **J**The serum level of LDL-C. **K** The serum level of TG. Data are expressed as mean ± standard error (n=6). Statistical significance is indicated as follows: ##p< 0.005, ####p < 0.0001 vs. NC; *p < 0.05, **p< 0.005, ***p < 0.001, ****p < 0.0001 vs. MC. ns indicates P>0.05.

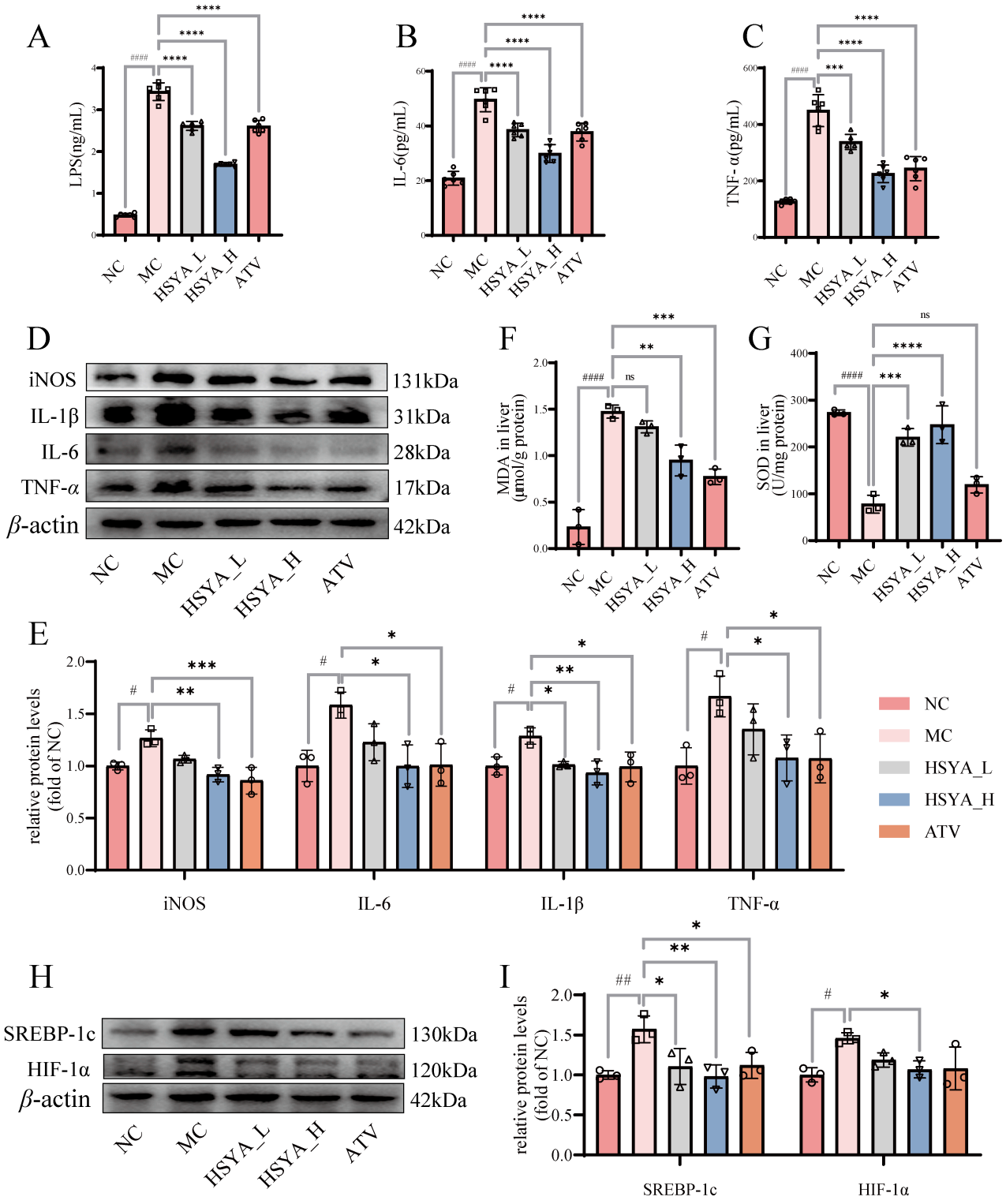


Figure 3

HSYA can alleviate hepatic steatosis, oxidative stress and inflammatory response induced by HFD in mice. **A** Serum LPS level; **B-C** Levels of serum inflammatory factors IL-6 and TNF-α (n=6); **D-E** Protein expression levels of iNOS, IL-1β, IL-6 and TNF-α in the liver detected by Western blot; **F-G** MDA level and SOD activity in liver tissue; H-I: Expression levels of SREBP-1c and HIF-1α proteins in the liver detected by Western blot. All data were analyzed using one-way ANOVA, and the results were expressed as mean ±

standard error. #$p < 0.05$, ##$p < 0.005$, ####$p < 0.0001$ vs. NC; *$p < 0.05$, **$p < 0.005$, ***$p < 0.001$, ****$p < 0.0001$ vs. MC. ns indicates $P>0.05$. Uncropped blots/gels are provided in Fig. S2.

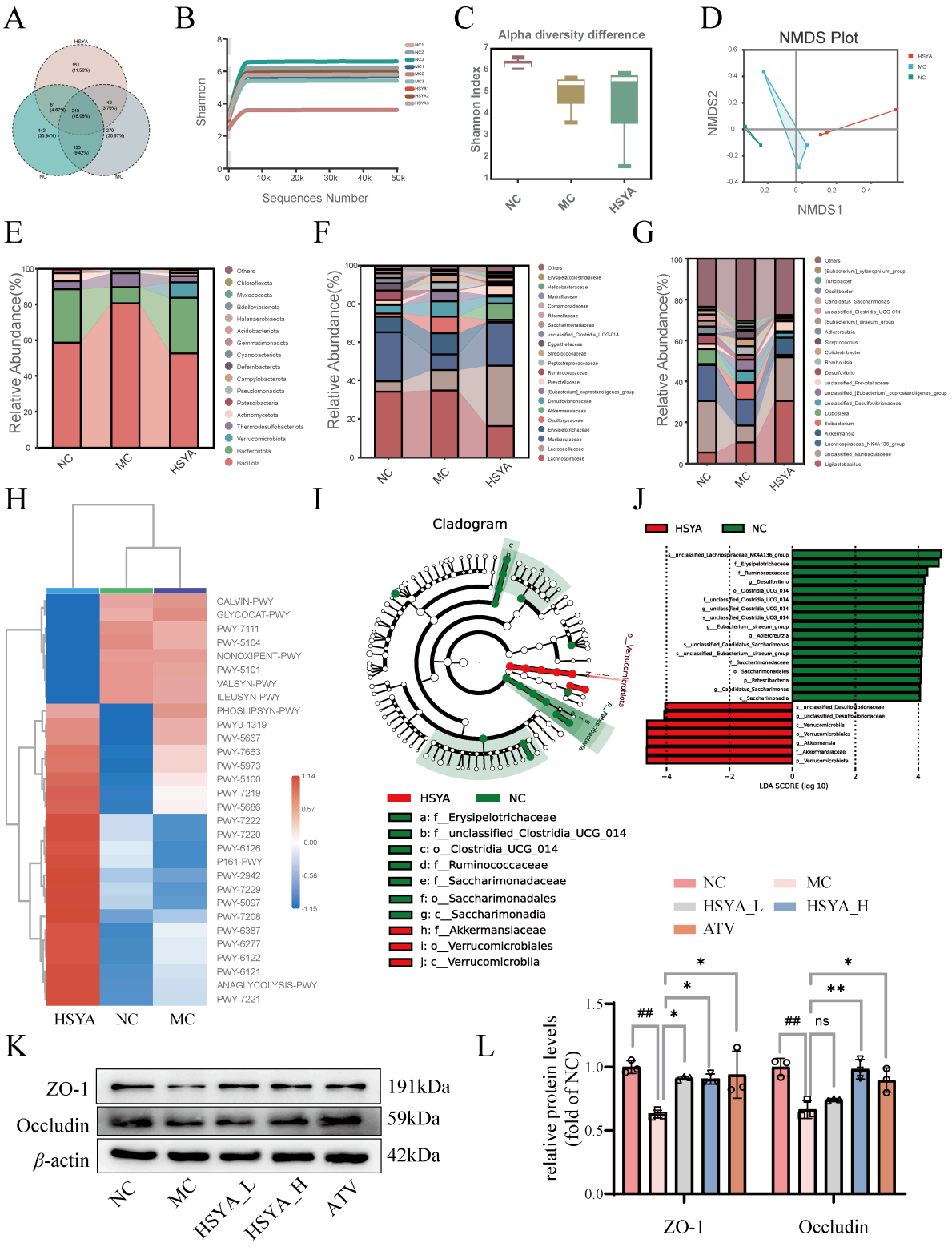


Figure 4

HSYA modulates gut microbiota composition and intestinal barrier integrity. **A** Venn diagram of OTUs. **B** Shannon rarefaction curve. **C** α diversity analysis. **D** NMDS analysis based on weighted Unifrac

distances. **E-G**Changes in gut microbiota at the phylum, family and genus levels. **H** PICRUSt2 functional prediction analysis. **I-J** LEfSe cladogram showing differentially abundant bacterial taxa. **K-L** Protein expression of ZO-1 and Occludin in colon tissues. Statistical analyses are presented as mean ± SEM. ##*P* < 0.01 vs. NC; **P* < 0.05, ***P* < 0.01 vs. MC; ns, *P* >0.05. Uncropped blots/gels are provided in Fig. S2.

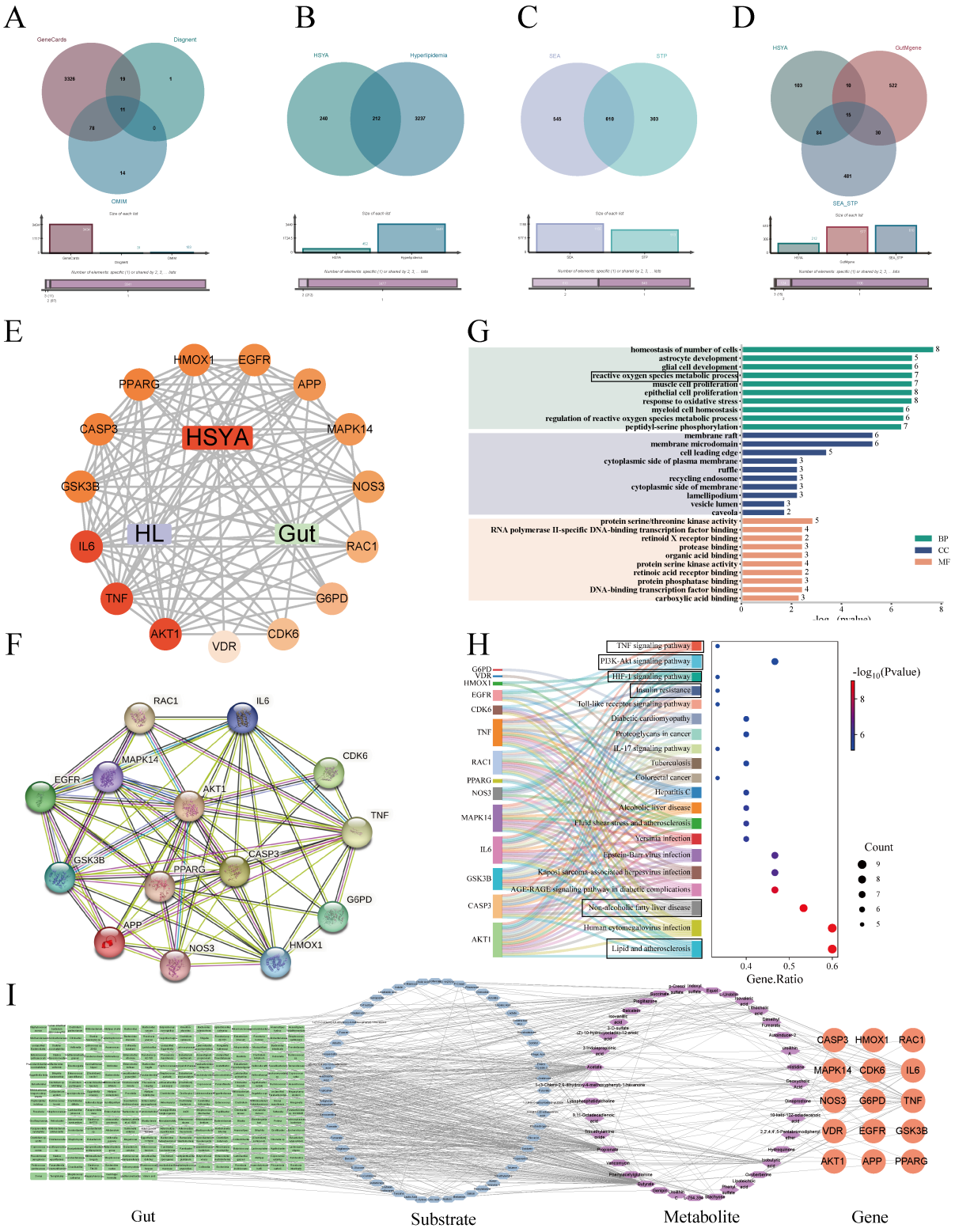


Figure 5

Network pharmacological analysis of HSYA-HL-Gut. **A** The HL targets of each database, **B** The common targets of HSYA and HL, **C** The common targets of gut microbiota metabolites predicted by SEA and STP databases. **D** The common target between the Metabolite-HL-HSYA and the human gut target. Analysis of **E-F** PPI network. GO-BP analysis and KEGG analysis of **G-H. I** Microbiota - substrate - metabolite - target network.

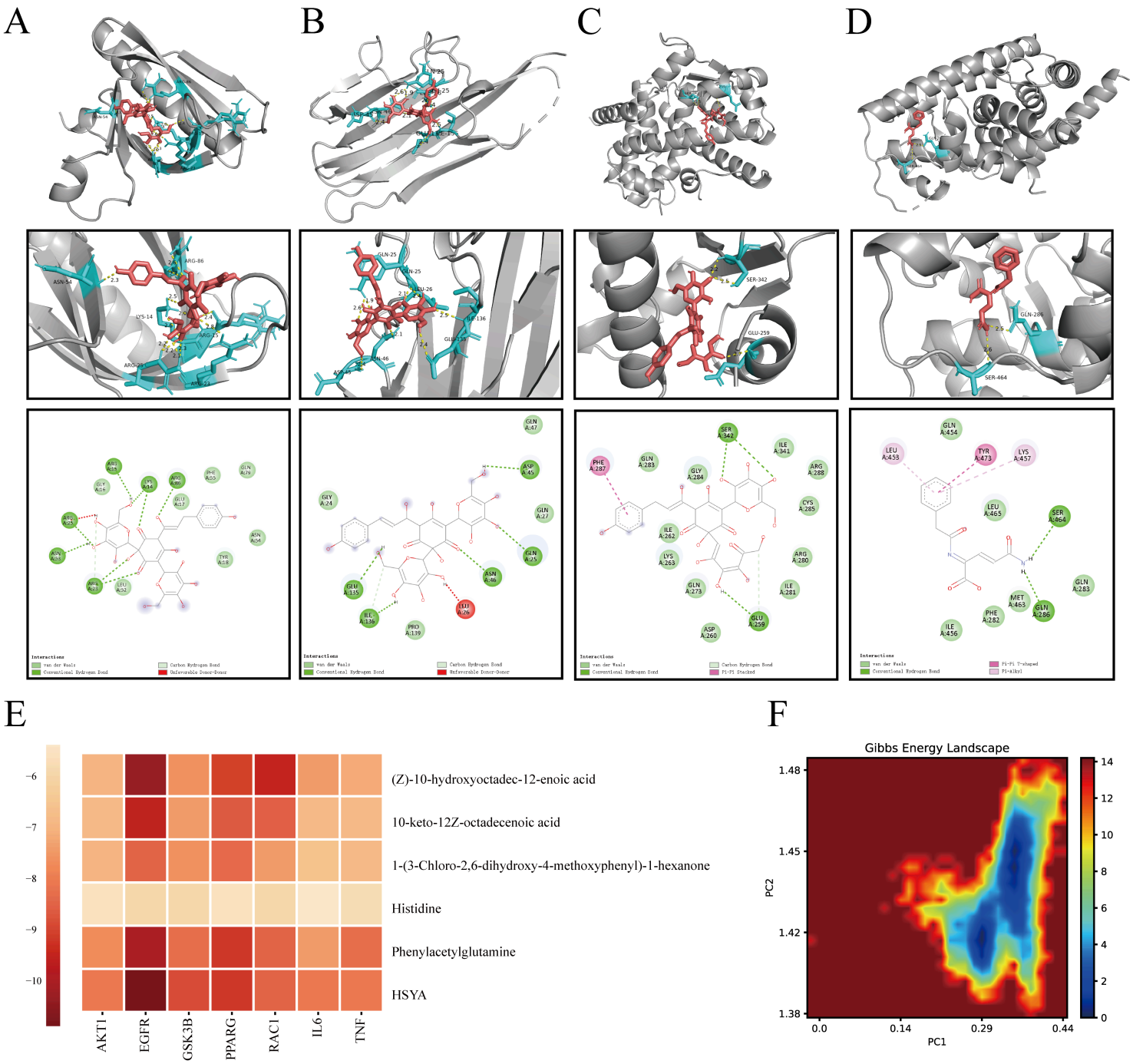


Figure 6

Molecular docking of core metabolites and HSYA with key proteins. **A** Visualization analysis of molecular docking between HSYA and AKT1; **B** Visualization analysis of molecular docking between HSYA and TNF-α; **C** Visualization analysis of molecular docking between HSYA and PPARA; **D** Visualization analysis

of molecular docking between Phenylacetylglutamine and PPARA; **E** Heatmap of molecular docking between key proteins and metabolites/HSYA; **F**MD Gibbs energy landscape illustrating the conformational distribution and stability of the HSYA-AKT1 complex.

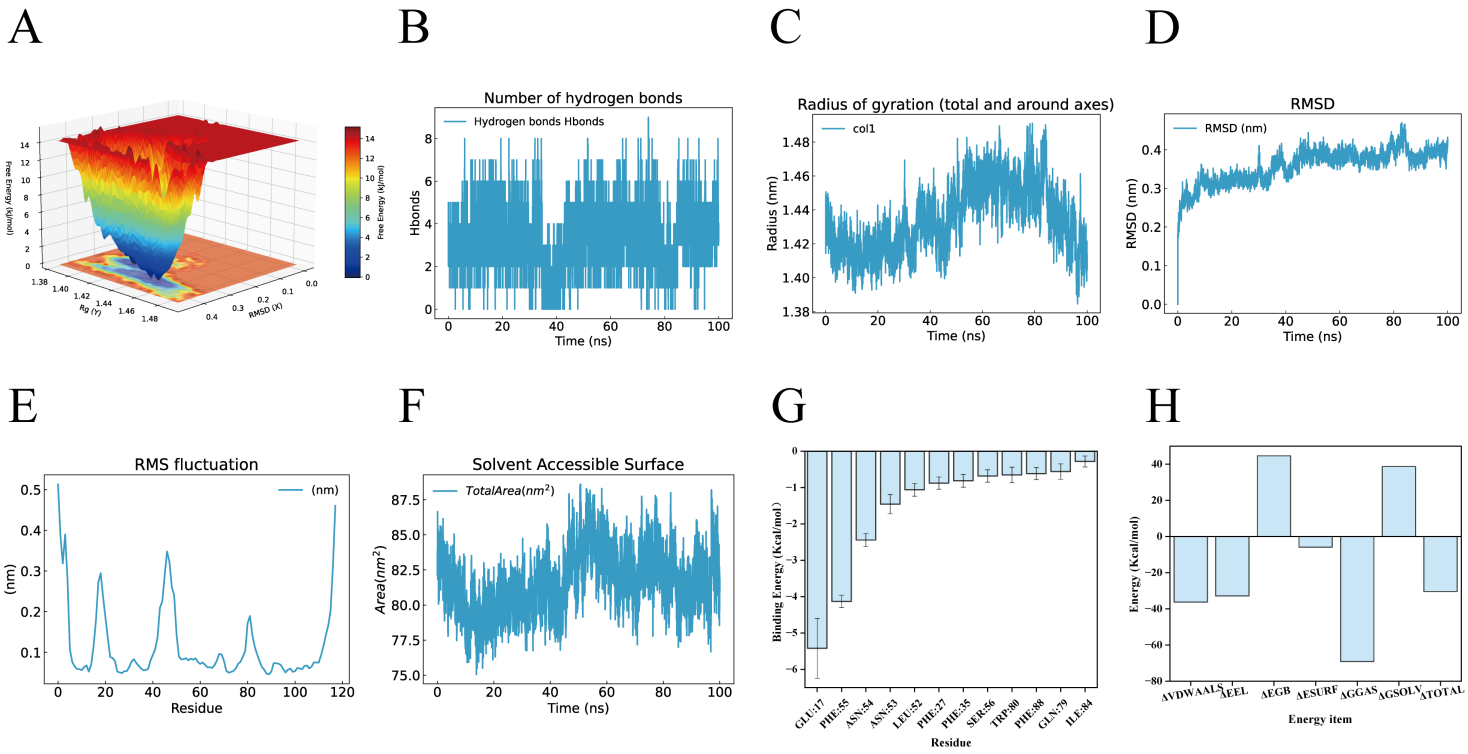


Figure 7

Molecular dynamics simulation analysis of HSYA binding to AKT1. **A** FEL of the HSYA-AKT1 complex, plotted as a function of RMSD and Rg, illustrating the conformational stability and dominant energy states during the simulation. **B** Time evolution of the number of hydrogen bonds between HSYA and AKT1, reflecting the stability of their interaction. **C** Rg of the protein backbone over time, indicating the compactness of the complex. **D** RMSD of the protein backbone, evaluating the overall structural stability throughout the simulation. **E** RMSF of residues, showing the flexibility of individual amino acids. **F** SASA of the complex, representing changes in protein surface exposure. **G** Per-residue energy decomposition analysis, identifying key residues contributing to the binding affinity. **H**Total binding free energy and its components (van der Waals energy, electrostatic energy, polar solvation energy, and non-polar solvation energy).

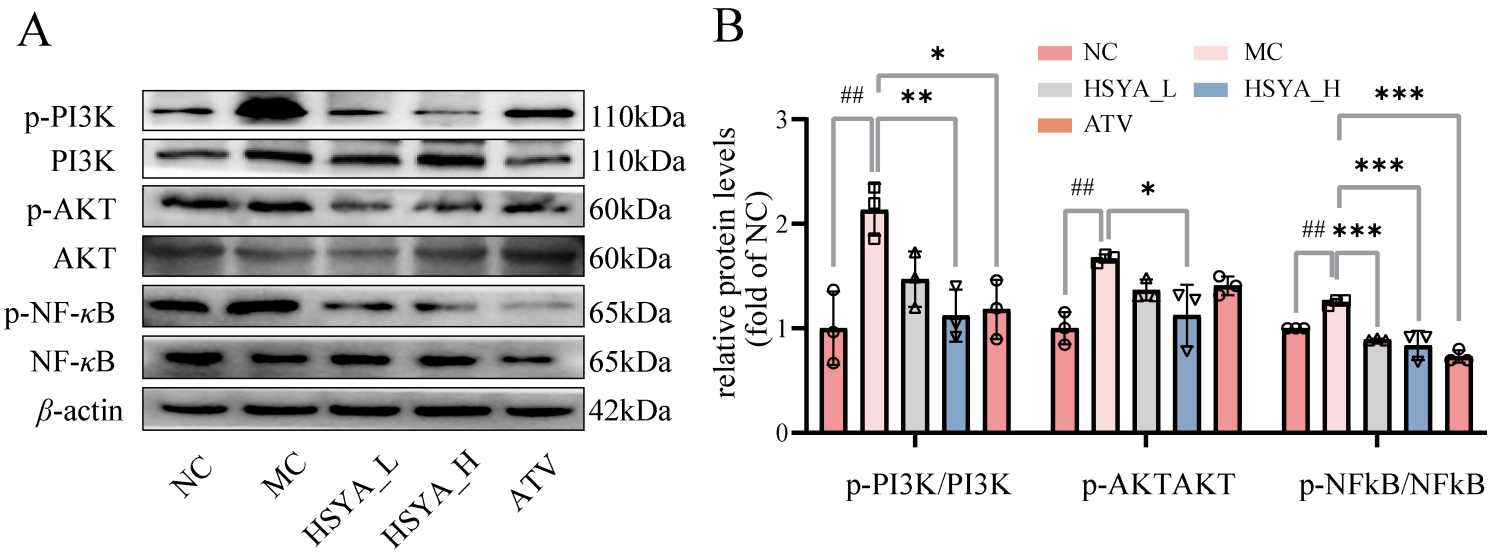


Figure 8

HSYA improves hepatic steatosis in mice by coordinating the expression of factors related to the PI3K/AKT signaling pathway. The protein levels of p-PI3K (p110), PI3K (p110), p-Akt, Akt, p-NFκB (p65) and NFκB (p65) in mice of each group and the quantitative analysis results were detected by **A-B** Western blotting; Data are expressed as mean ± standard deviation (n=3).##p< 0.005 vs. NC; *p < 0.05, **p < 0.005, *** p< 0.001 vs. MC. Uncropped blots/gels are provided in Fig. S3.

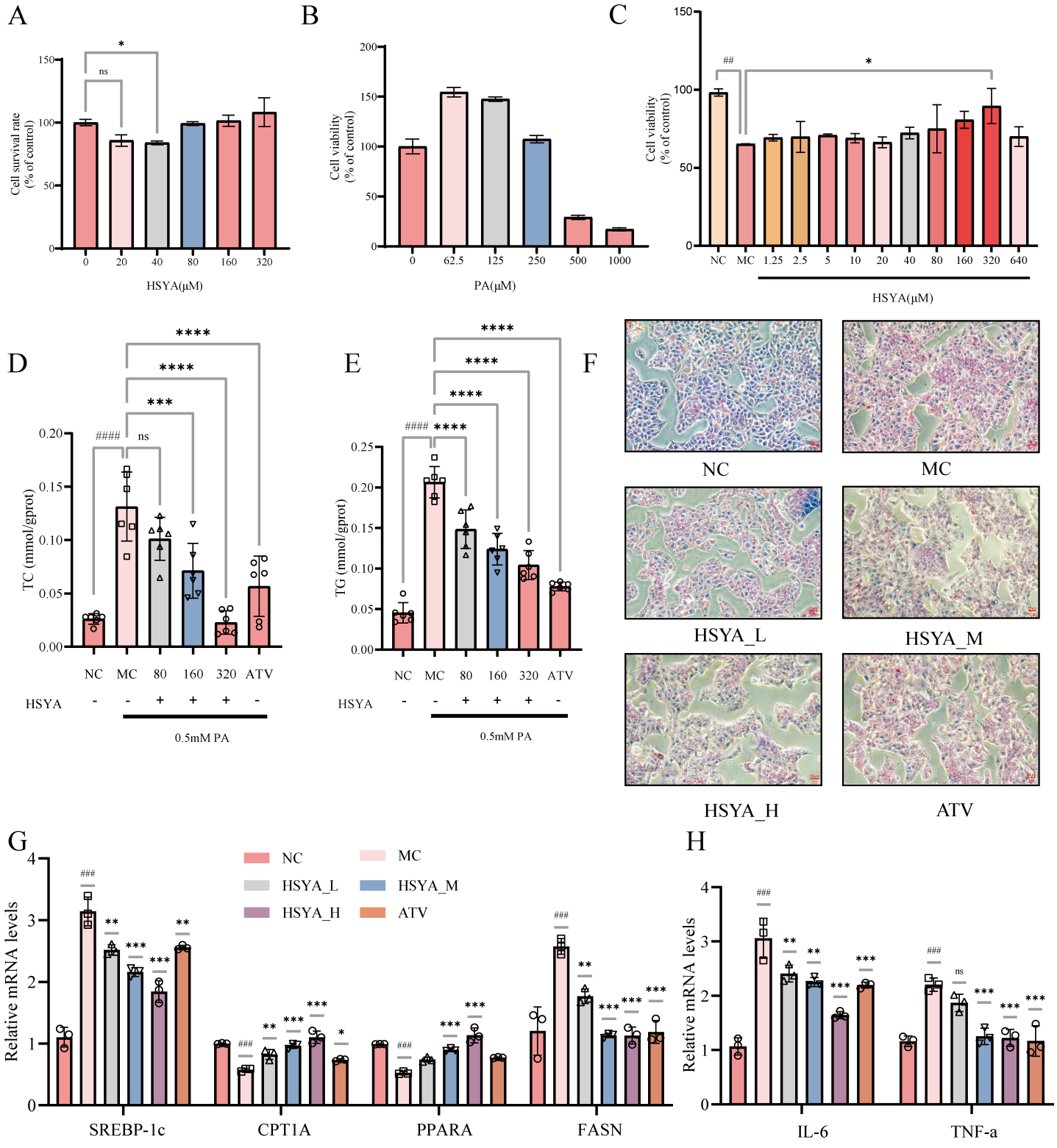


Figure 9

HSYA can alleviate the lipid toxicity of HepG2 cells induced by PA. **A** Cytotoxic effect of HSYA on HepG2 cells. **B** Effects of different concentrations of PA on the viability of HepG2 cells. **C** The protective effect of HSYA on cell damage induced by PA. The effect of **D-E** HSYA on the levels of TC and TG in HepG2 cells treated with PA. **F** Representative Oil Red O staining image (scale = 20 μm). **G** The effect of HSYA on the mRNA expression of lipid metabolism-related genes (*SREBP-1c*, *CPT1A*, *PPARA* and *FASN*) in

HepG2 cells treated with PA. **H** The effect of HSYA on the mRNA expression of inflammatory factors (*IL-6*, *TNF-α*) in HepG2 cells treated with PA. The data are expressed as mean ± standard deviation (n=3). ##$p < 0.005$, ###$p < 0.001$ vs. NC; *$p < 0.05$, **$p < 0.005$, ***$p < 0.001$, ****$p < 0.0001$ vs. MC (0.5 mM PA). ns stands for $P > 0.05$.

Supplementary Files

This is a list of supplementary files associated with this preprint. Click to download.

- supplementaryfile1.docx
- supplementaryfile1d1.docx
- GraphicalAbstract.docx